JGR Solid Earth

RESEARCH ARTICLE
10.1029/2023JB028411

Intermittent Criticality Multi-Scale Processes Leading to Large Slip Events on Rough Laboratory Faults

Grzegorz Kwiatek[1], Patricia Martínez-Garzón[1], Thomas Goebel[2], Marco Bohnhoff[1,3], Yehuda Ben-Zion[4], and Georg Dresen[1,5]

[1]Helmholtz Centre Potsdam, GFZ German Research Centre for Geosciences, Potsdam, Germany, [2]Department of Earth Sciences, Memphis Center for Earthquake Research and Information, University of Memphis, Memphis, TN, USA, [3]Free University Berlin, Institute of Geological Sciences, Berlin, Germany, [4]Department of Earth Sciences and Statewide California Earthquake Center, University of Southern California, Los Angeles, CA, USA, [5]Institute of Earth and Environmental Sciences, University of Potsdam, Potsdam, Germany

Key Points:

- We study preparatory processes preceding large slip events on rough laboratory faults using seismo-mechanical features derived from AE data
- The analysis highlights multi-scale rapidly evolving damage, roughness and stress changes along the fault surface
- Intermittent criticality marked by evolving stress correlations on different length scales can explain the observed patterns leading to large labquakes

Supporting Information:

Supporting Information may be found in the online version of this article.

Correspondence to:

G. Kwiatek,
kwiatek@gfz-potsdam.de

Citation:

Kwiatek, G., Martínez-Garzón, P., Goebel, T., Bohnhoff, M., Ben-Zion, Y., & Dresen, G. (2024). Intermittent criticality multi-scale processes leading to large slip events on rough laboratory faults. *Journal of Geophysical Research: Solid Earth*, *129*, e2023JB028411. https://doi.org/10.1029/2023JB028411

Received 3 DEC 2023
Accepted 15 FEB 2024

Author Contributions:

Conceptualization: Grzegorz Kwiatek
Formal analysis: Grzegorz Kwiatek, Patricia Martínez-Garzón
Funding acquisition: Marco Bohnhoff
Methodology: Grzegorz Kwiatek, Patricia Martínez-Garzón, Yehuda Ben-Zion
Resources: Thomas Goebel
Supervision: Yehuda Ben-Zion, Georg Dresen
Writing – original draft: Grzegorz Kwiatek

Abstract We discuss data of three laboratory stick-slip experiments on Westerly Granite samples performed at elevated confining pressure and constant displacement rate on rough fracture surfaces. The experiments produced complex slip patterns including fast and slow ruptures with large and small fault slips, as well as failure events on the fault surface producing acoustic emission bursts without externally-detectable stress drop. Preparatory processes leading to large slips were tracked with an ensemble of ten seismo-mechanical and statistical parameters characterizing local and global damage and stress evolution, localization and clustering processes, as well as event interactions. We decompose complex spatio-temporal trends in the lab-quake characteristics and identify persistent effects of evolving fault roughness and damage at different length scales, and local stress evolution approaching large events. The observed trends highlight labquake localization processes on different spatial and temporal scales. The preparatory process of large slip events includes smaller events marked by confined bursts of acoustic emission activity that collectively prepare the fault surface for a system-wide failure by conditioning the large-scale stress field. Our results are consistent overall with an evolving process of intermittent criticality leading to large failure events, and may contribute to improved forecasting of large natural earthquakes.

Plain Language Summary We discuss failure events in laboratory experiments on a rough fault performed at pressures existing in the Earth's crust. The laboratory faults were subjected to constant displacement resulting in short-lasting slips of their fault surface. We observe complex slip patterns including fast/slow ruptures with large/small fault slips. Very small slips on the fault surface were observed only with acoustic emission activity, representing tiny earthquakes of sub-mm size that produce elastic waveforms that can be recorded with piezo sensors. Using parameters derived from acoustic emission data, we analyzed physical processes leading to large slip events of the lab fault surface, an equivalent of a large earthquake in nature. Our parameters characterize local and global damage, stress, as well as interactions of small fractures before the labquake. We identify evolving fault roughness at different length scales, and find that the preparatory processes preceding lab quakes are facilitated by small earthquakes marked with bursts of acoustic emission activity. These bursts indicate ruptures of individual fault patches, which then interact and collectively prepare the fault surface for the labquake. Our results provide a set of physics-based parameters describing complex processes leading to lab slip events that may allow to improve earthquake forecasting along natural faults.

1. Introduction

Fault processes leading to large earthquakes have occasionally been observed to produce foreshock activity and aseismic transients, sometimes lasting months or even years prior to the main shock (Bouchon et al., 2013; Kato et al., 2012; Durand et al., 2020; Kwiatek et al., 2023; Schurr et al., 2014; Meng & Fan, 2021). Seismic and aseismic precursors signifying fault damage evolution and progressive localization toward large dynamic ruptures are not well understood due to limited availability and resolution of seismic data and widely varying structures and properties of fault zones (e.g., Ben-Zion, 2008, and references therein). The role of precursory observables during the preparatory process before earthquakes and their potential use for forecasting remains controversial (Bakun et al., 2005; Geller et al., 1997; Mignan, 2014; Ogata & Katsura, 2012; Wu et al., 2013). Existing physical

Writing – review & editing: Grzegorz Kwiatek, Patricia Martínez-Garzón, Thomas Goebel, Marco Bohnhoff, Yehuda Ben-Zion, Georg Dresen

models describing the preparation and nucleation process on large pre-existing faults motivated by field and laboratory studies (Dieterich, 1978; Ellsworth & Beroza, 1995; Kato & Ben-Zion, 2021; McLaskey, 2019; Ohnaka, 1992) converge toward a combination of processes including accelerating preslip and, in some cases, cascading foreshocks. However, fault heterogeneity and structural variability of fault zones result in rich and varying observational phenomena, that often defy clear interpretation. Thus, seismic hazard assessment and earthquake forecasting still largely rely on probabilistic approaches (Hirose et al., 2021; Lippiello et al., 2019; Mizrahi et al., 2023; Ogata, 1999). The observation of a plethora of physical preparatory processes requires high-resolution monitoring of both seismic and aseismic failures using frequency bands that are hardly achievable in nature.

Laboratory experiments performed on intact and faulted rock samples with varying loading conditions have provided a wealth of observations characterizing the effects of roughness, gouge material, loading rate, effective normal stress, and stiffness ratio of the fault and loading system on long-term deformation leading to failure (Gounon et al., 2022; Guérin-Marthe et al., 2019; Latour et al., 2013; Leeman et al., 2018; Mclaskey & Yamashita, 2017; Morad et al., 2022; Scuderi et al., 2020). Motivated by experimental results, various studies (Ben-Zion & Rice, 1997; Dieterich & Kilgore, 1996; Latour et al., 2013; Ohnaka, 1992; Ohnaka & Shen, 1999) have suggested to separate the preparatory phase into a quasi-static phase and an accelerating phase producing dynamic slip (e.g., Okubo & Dieterich, 1984). This transition is often only loosely defined by the onset of a local or system-wide decrease in shear stress leading to an abrupt stress drop or transition in rupture velocity, and an overall change of energy flux into the rupture front tip. In a complex and heterogeneous fault zone, the preparation phase may be long-lasting. The transition towards nucleation of a large rupture involves a localization process, distributed creep transients and collective failure of a range of asperities (de Geus et al., 2019; Lebihain et al., 2021; McBeck et al., 2022; Yamashita et al., 2021). These processes lead to redistribution of stresses along the fault zone at different length scales, reflecting the multi-scale evolution of roughness at the level of granular material forming the fault zone, cm-scale asperities and large-scale structural inhomogeneities.

The multi-scale preparatory processes before large laboratory slip events are typically accompanied by Acoustic Emission (AE) activity that allows monitoring key seismo-mechanical processes and local stress evolution during the deformation cycle. Parameters derived from AE data showed changes in clustering and localization of AE hypocenters, AE magnitude-frequency distributions, ultrasonic velocities, inter-event triggering and other statistical attributes approaching failure (Bolton et al., 2023; Davidsen et al., 2017, 2021; Goebel et al., 2012, 2013, 2014; Kwiatek, Goebel, & Dresen, 2014; Lockner, 1993; Main, 1991, 1992; Scuderi et al., 2017; Zang et al., 1998). Typically, AE-derived parameters from stick-slip cycles exhibit general trends, which are punctuated and partially reversed by large failure events. Although the observed trends for some parameters during the preparatory slip indicate progressive damage and localization, estimating time-to-failure is still challenging.

In recent years, earthquake forecasting made a leap using new opportunities provided by Artificial Intelligence (AI) techniques. These techniques demonstrated an ability to predict time-to-failure in direct shear laboratory tests on smooth faults (Johnson et al., 2021), as well as on analog models, natural and induced seismicity, and synthetic modeling (e.g., Corbi et al., 2019; Johnson et al., 2021; McBeck et al., 2021). Such studies use a number of potential precursory parameters derived from seismic waveforms or earthquake catalogs (see, e.g., Hulbert et al., 2019; Lubbers et al., 2018; Picozzi & Iaccarino, 2021; Rouet-Leduc et al., 2017). Johnson et al. (2021) noted that successful cross-scale earthquake forecasting requires generalization of predictive models and a better physical understanding of input and output parameters. The former involves extension of the predictive AI-aided modeling to studies of rough faults, whereas the latter requires a clear linking of AE-derived precursory parameters with observable damage and stress evolution on different spatio-temporal scales.

In this study we employ large AE datasets from laboratory stick-slip experiments involving a series of tests performed on rough pre-fractured faults (e.g., Goebel et al., 2012, 2013, 2014). The experiments produced complex slip patterns including large and small slips of the fault surface (characterized by large and small stress drops), and confined slips (with stress drops not measurable with the internal load cell) accompanied by AE data bursts. The multi-scale preparatory processes preceding system-wide slip events are analyzed with a set of physics-motivated AE-based features characterizing the seismo-mechanical spatio-temporal processes occurring on the fault. These include parameters describing damage and stress evolution, localization and clustering, event interactions, and local micromechanics and stress heterogeneity. We decompose the observed trends and discuss

them in the context of roughness evolution at different spatial scales, a crossplay of local and global damage, and multi-scale stress evolution when approaching a system-size event.

2. Data and Methods

2.1. Experimental Setup and Acoustic Emission Monitoring

Three triaxial stick-slip tests WgN04, WgN05 and WgN07 were conducted on cylindrical samples of Westerly Granite with dimensions of 40 mm diameter × 107 mm length (Goebel et al., 2012, 2013, 2014, 2015). Samples were prepared with a 2.5 cm deep notch inclined at 30° to the cylinder axis to guide formation of a shear fracture. The samples were first oven-dried at 100°C and subsequently encapsulated in a rubber sleeve to prevent the intrusion of the confining medium (oil). The specimens were fractured at 75 MPa confining pressure creating naturally fractured rough fault surface. To perform a series of subsequent stick-slip experiments, the faults were locked by increasing the confining pressure to 150 MPa. For the initial fracture and subsequent stick slip tests, the samples were loaded axially using a constant displacement rate of 0.02 mm/min = 0.33 μm/s. Subsequent axial loading cycles were applied by advancing the piston at constant displacement rate resulting in an axial strain rate $3 \times 10^{-6}\ s^{-1}$. Displacement and axial force were recorded using a linear variable displacement transducer fixed to the piston and external/internal load cells, respectively.

We performed a series of tests on the three different Westerly granite samples WgN04, WgN05, and WgN07 containing rough faults (Goebel et al., 2012, 2013, 2014, 2015) but here we present data from an illustrative stick-slip test (WgN05) that was further studied in greater detail in Dresen et al. (2020) and Blanke et al. (2021). The recorded AE data, mechanical data and output parametric data from all three experiments are available in the associated data publication (Kwiatek & Goebel, 2024; see also Figures S5-S6 in Supporting Information S1 and Open Data section). The fault roughness in these experiments caused a complex stick-slip pattern with a variety of stress drops including five large slip events with large stress drops (LSD) of >100 MPa preceded by a varying number of events with smaller slip and small stress drops (SSD), as determined from the axial stress data in Goebel et al. (2013, 2015). They are shown in Figure 1 and Figures S5-S6 in Supporting Information S1. Both LSDs and SSDs are accompanied by a large clipped signal on the AE data, representing large laboratory events (see, e.g., Figure 3 in Goebel et al., 2012).

Loading and stick-slip events produced AEs, here indicating ∼ mm-scale fracturing and frictional processes occurring on the grain scale (cf. Blanke et al., 2021). AE activity was recorded by 16 AE sensors with resonant frequency 2 MHz embedded in brass housings and glued directly to the specimen surface, securing an almost complete azimuthal coverage of AE events. The event waveforms were recorded in triggered mode at 10 MHz sampling rate with 16-bit amplitude resolution. Throughout the experiment, repetitive *P*-wave velocity measurements were performed using ultrasonic transmission providing a time-dependent velocity model composed of five equally-spaced horizontal layers (with associated velocity) and single measurement of averaged vertical velocity (Stanchits et al., 2006). The velocity model was updated every 30 s during the course of the experiment.

2.2. Mechanical Behavior and AE Response

We now describe the evolution of mechanical parameters and associated AE response for an illustrative sample WgN05 following the conventions presented already and discussed in Goebel et al. (2012, 2013, 2014, 2015). Mechanical evolution for samples WgN04 and WgN07 is presented in the supplementary information (Figures S5-S6 in Supporting Information S1), and the input catalog data are available in the associated data publication (Kwiatek & Goebel, 2024). Sample WgN05 displayed five large stress drops ΔS (measured in the axial S_1 direction) of $\Delta S > 100$ MPa, measurable slip duration of 0.2–0.4 s and slip velocity (corrected for machine stiffness) of at least 1.2–1.6 mm/s, which is at least 1,000 times larger than the applied loading rates (cf. Section 2.1, Figure 1, Table S1 in Supporting Information S1). Note that peak slip velocities for LSDs were not resolved due to the limited sampling rate of the geomechanical data (10 Hz). All LSDs were followed by rapid initial reloading lasting ca. 50 s and a longer period of almost linear stress increase lasting typically no more than 1,000 s. Further axial displacement beyond a yield point was accommodated by plastic deformation along the fault zone and in its surroundings (cf. Dresen et al., 2020). We attribute most of the deformation during this part of the loading to shear-enhanced compaction of the granular material forming the fault gouge (Goebel et al., 2017; Kwiatek, Goebel, & Dresen, 2014), as illuminated by the AE activity spreading over the whole fault surface (Figures 1e and 1h).

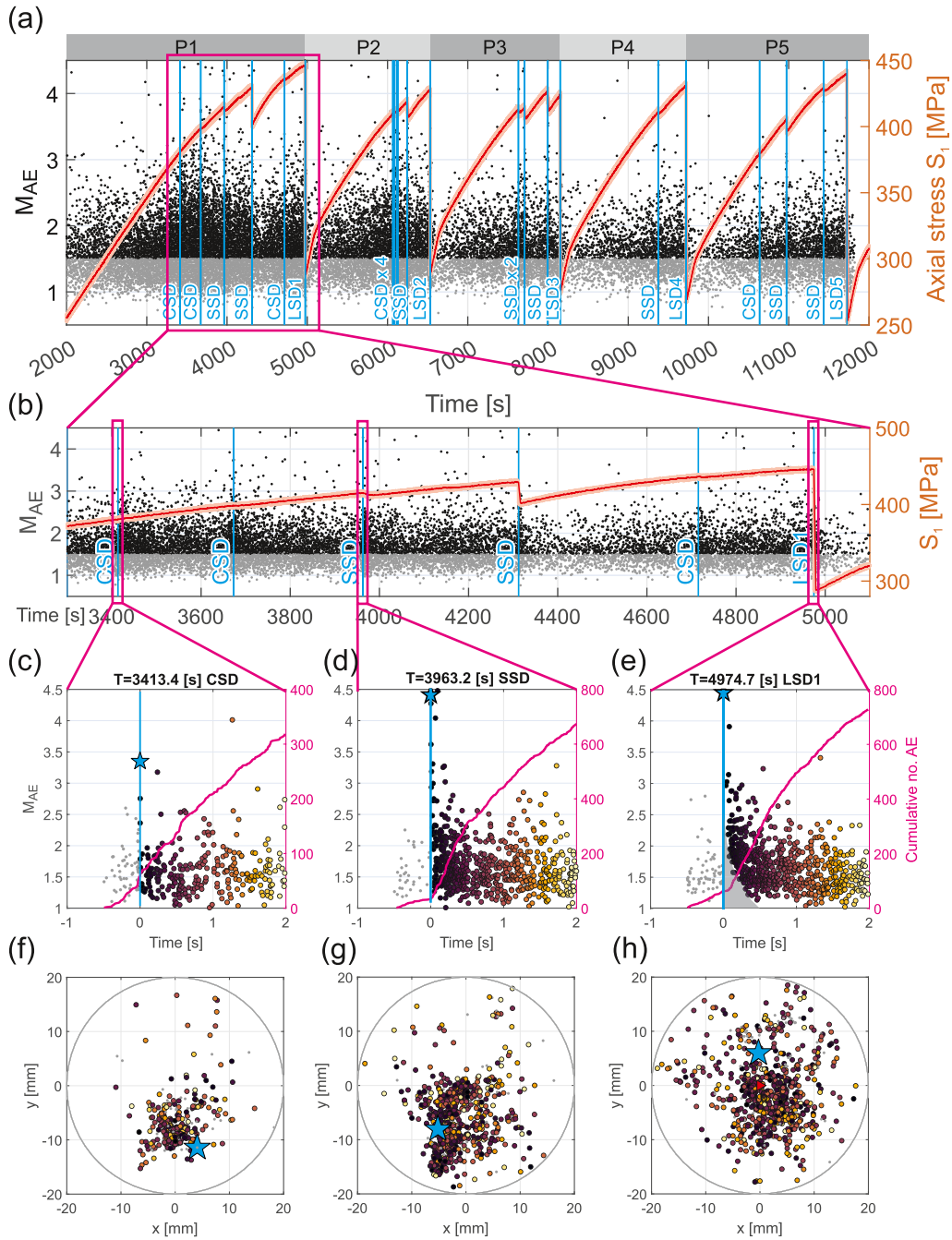

Figure 1. Overview of mechanical data, AE activity and stick-slip processes at different temporal scales occurring during the experiment. (a, b): AE magnitudes (black dots, left axis) and axial load (red solid curve, right axis). Onsets of large (LSD), small (SSD), and confined slips events (CSD, see Section 2.2 for details), the latter not reflected in axial stress data, are marked with vertical azure lines; (b): zoom-in of the time period between 3400 s and 5000 s covering the preparatory processes ahead of the LSD1; (c–h): zoom-in of the time window framing the representative confined slip event CSD (c, f), small slip event SSD (d, g) and large slip event LSD (e, h) with AE magnitudes color-coded with time; (f, g, h): Corresponding top-view of the AE activity with blue stars marking the location of the AE event initiating the slip. Gray area in (e) denotes short-lasting saturation of the recording system with low-frequency noise from the slip event limiting the detection of individual AE events (see text for details) following the occurrence of LSD. Remaining time windows framing slip events are shown in Figure S1 in Supporting Information S1.

Cm-scale roughness of the fault surface (cf. Figure S7 in Supporting Information S1) results in multiple small slip events with low stress drops (SSDs), as defined in for example, Goebel et al. (2012), which typically occur at elevated axial stress with $S_1 > 400$ MPa. The AE activity associated with these SSDs is distributed over significant parts or the entire fault surface (Figures 1d and 1g). Stress drops of SSDs range $1 < \Delta S < 20$ MPa and slip velocities range <0.05–0.2 mm/s (Table S1 in Supporting Information S1). The lower observable limit of SSDs' stress drops and slip velocity is due to the periodic noise of stress measurements caused by the servo-controlled triaxial loading system.

The macroscopic displacement and stress drop recordings of LSDs and SSDs indicate detectable and relative movement of fault-bounding blocks across the entire fault surface (Movie S1 in Supporting Information S1). The nucleation of both LSDs and SSDs is associated with extremely large AE events with clipped waveforms following the first P-wave arrival (e.g., Goebel et al., 2012; Figure 3; Goebel et al., 2015; Figure 5) and followed by a long coda wave indicating slip over the surface. This coda leads to a temporally higher AE event detection threshold due to low-frequency noise resulting from comminution and shearing of granular material and debris forming the fault surface while the fault is slipping (gray area in Figure 1e). The duration of the AE system saturation time period lasts 20–120 ms and qualitatively scales with the duration of macroscopic slip and stress drop magnitude (cf. Table S1 in Supporting Information S1). The enhanced low-frequency noise is expected to mask very early AE events directly following the LSDs.

In addition to LSD and SSD events resulting in externally measurable axial stress drops, we visually identified short-lasting bursts in AE activity due to slips confined in the sample that were mostly not recorded in the mechanical data (i.e., the externally measured axial stress drop is $\Delta S < 1$ MPa). These local confined slips (CSD) with no externally measured stress drop were attributed to local asperity failures providing a significant AE footprint with very localized AE activity that is most prominent in the early stick-slip cycles (cf. Figures 1c and 1f; Movie S1 in Supporting Information S1; see also Goebel et al., 2012, 2015). Like LSD and SSD, each CSD is also associated with a large AE event followed by smaller AEs (AE aftershocks) and occasionally preceded by increasing AE activity (AE foreshocks, see results section for details).

2.3. AE Catalog Development

The development of an AE catalog from the experimental data is an upgraded procedure originally developed by Stanchits et al. (2006). Here, we summarize key and new processing steps relevant for evaluating the time-dependent AE characteristics.

The first P-wave arrivals of AE events were picked automatically using the Akaike Information criterion followed by pick refinement using the modified Convolutional Neural Network picker (Ross et al., 2018) trained on past AE data sets. Based on a time-dependent quasi-anisotropic velocity model, the resolved picks were used to invert for hypocenter locations and origin time using a grid search algorithm paired with the Coyote optimization algorithm (Pierezan & Dos Santos Coelho, 2018). The hypocenter location accuracy is estimated to be about ±2 mm, constrained, in part, by the selected Root-Mean-Square Deviation (RMSD) of travel time residuals (for the following analysis we selected locations with RMSD < 0.5 μs). Then, the first *P*-wave amplitudes were corrected for hypocentral distance and incidence angle and for the coupling quality of AE sensors using an ultrasonic calibration technique (Kwiatek, Charalampidou, et al., 2014). The average AE amplitude $\overline{A_{\mathrm{AE}}}$ and AE magnitude M_{AE} were calculated from first P-wave amplitudes (Zang et al., 1998):

$$\overline{A_{\mathrm{AE}}} = \frac{1}{n}\left(\sum_{i=1}^{n}(A_i R_i)^2\right)^{0.5}, \tag{1}$$

$$M_{\mathrm{AE}} = log_{10}\left(\overline{A_{\mathrm{AE}}}\right), \tag{2}$$

where A_i and R_i are corrected first P-wave amplitude and source-receiver distance for sensor i, respectively (cf. Dresen et al., 2020). The here used AE magnitude reveals relative size differences between AE events but it is not directly calibrated to the physical size of the events (cf. Blanke et al., 2021; Goodfellow & Young, 2014; McLaskey et al., 2014; Yoshimitsu et al., 2014).

For each AE event, a full moment tensor (FMT) inversion was performed using the hybridMT software and first P-wave amplitudes and durations of the first P-wave pulses (Kwiatek et al., 2016; Martínez-Garzón et al., 2017) corrected for coupling quality and incidence angle (Kwiatek, Charalampidou, et al., 2014). The resulting FMTs were decomposed into isotropic and deviatoric parts (e.g., Vavryčuk, 2001, 2014). From the deviatoric part of the FMTs, we extracted the P-, T-, and B- axes directions (azimuths and plunges) and slip directions. A P- (T-, B-) axis plunge equal to 90° and 0° corresponds to the direction of maximum axial compression S_1 and the direction perpendicular to it, respectively. The two sets of nodal plane parameters (strike, dip, rake) were extracted from the deviatoric part of the seismic FMT of each AE event.

The analyzed catalog from WgN05 sample contains $N = 310{,}815$ located AEs with $N(M_{AE} > M_{C,AE}) = 169{,}825$ above the magnitude of completeness $M_{C,AE} = 1.5$ estimated using the goodness-of-fit method (Wiemer & Wyss, 2000) assuming that 95% of the catalog is explained by the Gutenberg-Richter power law. The FMTs were strongly quality-constrained, first at the input data selection (we only accepted input data where amplitude could be measured at all sensors), and then using as an uncertainty measure the maximum value of the diagonal elements of the covariance matrix normalized by the average AE amplitude, ϵ (see details hybridMT documentation, Kwiatek et al. (2016). Assuming, $\epsilon < 0.1$ and $N_{\text{stations}} = 14$, this resulted in a strongly reduced number of N (FMT) = 17,963 high-quality FMTs. The resulting catalog containing origin time, AE location in the local Cartesian coordinate system of the sample, AE magnitude, FMT parameters including strike, dip, rake, the MT decomposition and orientation of P-, T-, and B- axes, as well as associated location and MT inversion uncertainties is available in an associated data publication (Kwiatek & Goebel, 2024).

2.4. Time Series of AE Parameters

For all three samples we analyzed the temporal evolution of a total of 10 parameters (features) derived from the AE catalog and defined onsets of informative changes of these parameters with regard to global damage and stress evolution and potential cross-correlations between different proxies. The selected parameters were utilized to characterize the development of local damage and stress evolution on and around the fault during the preparatory phases of five LSDs. The predictive AE-modeling of the time-to-failure, aggregating the input data from all three experiments, as well as unsupervised classification of the preparatory phase are subjects of separate manuscripts (Karimpouli et al., 2023, 2024).

The temporal evolution of all AE parameters was calculated using sliding time windows of different lengths (ranging 1%–12% of the average length between consecutive LSDs, see Table 1) to better represent the development of short- and long-term processes. The calculated parameter values were assigned to the origin time of the last AE event included in each time window. We ignored time windows which overlap with the occurrence of LSDs to avoid mixing precursory AEs with those following LSD. In the following, we describe the 10 different AE parameters listed in Table 1 and subsequently used for tracking the preparatory processes.

1. **AE event rate:** The AE event rate $\dot{N}$ (unit: [1/s]) has been calculated for the catalog of events with $M_{AE} > M_{AE,C}$ as the number of AEs divided by the duration of the moving time window. It represents the intensity of seismic activity across the whole fault surface and characterizes the damage (cf. Goebel et al., 2014).
2. **b-value:** The slope from the magnitude-frequency Gutenberg-Richter (GR) relation indicates the proportion between the number of small and large AE events in a selected population. The b-value is calculated from AE events with magnitudes above the magnitude of completeness $M_{AE} > M_{AE,C}$ using the maximum likelihood method while including a correction for the histogram bin size (e.g., Lasocki & Papadimitriou, 2006). Changes in b-values are thought to be governed by rock damage evolution (e.g., Main, 1991), changes in local stress (Scholz, 1968; Schorlemmer et al., 2005), and geometric complexity and roughness (Goebel et al., 2013, 2017).
3. **d-value:** The fractal dimension d from a population of AE hypocenters has been calculated using the boxcount algorithm (i.e., Minkowski–Bouligand dimension, see Moisy, 2022). We used quality-constrained hypocentral locations [X, Y, Z] with RSMD < 0.5 [μs]. The d-value characterizes the geometry of the AE spatial distribution of AE with $d = 3$, $d = 2$, and $d = 1$ corresponding to volumetric, planar and linear Euclidean distribution of AE hypocenters, respectively. Contrary to the d-value estimated using correlation integral, which is sensitive to point-clustering of the hypocentral locations, the box-counting method solely responds to the bulk geometry of AE hypocenter distribution.

Table 1
Parameters Characterizing the Temporal Evolution of Damage and Stress in the Sample

No.	Parameter	Symbol	Time windows [s]	Dimension sensitivity	Source/method
1	AE event rate	$\dot{N}$	23.5, 45, 90, 180	Time	AE catalog
2	b-value (maximum likelihood)	b	10, 30, 90, 180	Time-magnitude	
3	d-value (boxcounting)	d	45, 90, 180	Space-time	
4	Median proximity	$\hat{\eta}$	25, 50, 100	Space-time-magnitude	Clustering analysis
5	Proportion of foreshocks	p_{FO}			
6	Proportion of aftershocks	p_{AF}			
7	Proportion of mainshocks and singles	p_{MA}			
8	Median fault plane variability	$\widehat{\Psi_f}$	100, 200	Space-time	Focal mechanisms
9	Plunge of local maximum principal stress	$\delta_{\sigma 1}$	90, 180	Space-time	Stress tensor inversion
10	Local stress variability	$\widehat{\Psi_{\sigma ij}}$			

Note. Column 'dimension sensitivity' generalizes whether the particular parameter is sensitive to changes in time, space, magnitude, or their combination.

Clustering of AE events in space, time and magnitude domain: We identified clusters of AE events according to their space-time-magnitude nearest-neighbor proximity (Zaliapin & Ben-Zion, 2013a, 2013b; Zaliapin et al., 2008). Specifically, we investigated the proximity of an event j to an earlier event i in a combined space-time-magnitude domain (Baiesi & Paczuski, 2004) defined as:

$$\eta_{ij} = \left\{t_{ij}(r_{ij})^d 10^{-bm_i}\right\},\ t_{ij} > 0, \infty,\ t_{ij} \le 0, \tag{3}$$

where $t_{ij} = t_j - t_i$ and r_{ij} are the temporal and spatial distances between the earthquakes i and j, respectively, b is the b-value from the GR distribution, d is the fractal dimension, both estimated as described above, and m_i is the magnitude of the earlier event in time. The scalar proximity η_{ij} between events can be expressed as the product of its temporal and spatial components scaled by the magnitude of the earlier event i:

$$\eta_{ij} = T_{ij} \cdot R_{ij}, \tag{4}$$

with $T_{ij} = t_{ij}10^{-qbm_i}$ and $R_{ij} = (r_{ij})^d 10^{-(1-q)bm_i}, 0 \le q \le 1$. We fixed $q = 0.5$, providing equal magnitude weights to the scaled temporal and spatial distances. To estimate the spatial distance between events we used hypocentral locations. We denote η_j the shortest of the proximities between event j and all earlier events. The distributions of the nearest-neighbor proximities η_j in earthquake catalogs tend to be bimodal (Martínez-Garzón et al., 2019; Zaliapin & Ben-Zion, 2013a; Zaliapin & Ben-Zion, 2016). The mode with larger event proximities η_j corresponds to *background* Poissonian-like seismicity, while potentially appearing mode with smaller event proximities η_j indicates *clustered* events, that is, foreshocks and aftershocks (Zaliapin et al., 2008). The separation threshold between these two modes is estimated by fitting a Gaussian mixture model (Figure S2 in Supporting Information S1).

Using the above method, we identify AE clusters that are connected by proximity links smaller than the estimated threshold. Each AE connected to the parent by a link longer than the threshold is considered a *background* event and starts a new cluster. A *single* is a cluster that consists of one background event with no associated foreshocks or aftershocks, while multiple-event clusters are called *families*. The largest event in each cluster is called *mainshock*; all events within the cluster before or after the mainshock are called *fore/after-shocks* (see Figure 6 of Zaliapin & Ben-Zion, 2013a). Due to the short-term saturation of the AE recording system during large slip events LSD1–LSD5 (see more details in the results section), the clustering analyses have been performed separately for each phase P1–P5 (Figure 1a). This means that early aftershocks from previous slip for phases P2–P5 are not well resolved, biasing the separation between foreshocks, aftershocks, mainshocks and singles shortly after the LSDs.

The temporal changes in AE clustering properties occurring on grain-scales have been analyzed using a sliding time window. We calculated temporal evolution of four parameters, including the **(4) median proximity** parameter $\hat{\eta}$:

$$\hat{\eta} = median\{\eta_j\}, \quad (5)$$

defined as a median of the decimal logarithm scalar proximities (Equation 4) of AEs, and the fraction of AE **(5) foreshocks** (p_{FO}), **(6) aftershocks** (p_{AF}), and **(7) background (mainshocks and singles altogether)** (p_{MA}) in each examined time window (with $p_{AF} + p_{FO} + p_{MA} = 1$).

The **(8) median fault plane variability** $\widehat{\psi_f}$ characterizes the level of heterogeneity in the distribution of the focal mechanisms (Dresen et al., 2020; Goebel et al., 2017; Martínez-Garzón et al., 2016). This is a generalization of rotation angle between pairs of focal mechanisms (Kagan, 2007) applied to an ensemble of pairs of AEs with focal mechanism solutions located nearby. A small 3D rotation angle (<20°) between the P/T/B axes of two mechanisms indicates a high degree of similarity, and 0° means they are identical.

We compute the spatial variability of focal mechanism similarity across the laboratory fault and rock sample. Spatial variability is determined from 20 nearest AE neighbors located within $R < 10$ mm of the specific AE event by calculating the respective median 3D rotation angle between all focal mechanism pairs (e.g., for 20 AE focal mechanisms there are 190 pairs). This procedure was repeated for each AE event to resolve the spatial heterogeneity/similarity of focal mechanism variability across the whole fault plane. The focal mechanism variability for a particular time window was then estimated as the median of locally calculated values.

(9) Plunge of local maximum principal stress $\delta\sigma_1$ and (10) local stress (orientation) variability $\Psi\sigma ij$: Using calculated MTs we performed a linear stress tensor inversion using the STRESSINVERSE package (Vavryčuk, 2014). We follow the sign convention that compressive stress is positive with $S_1 > S_2 > S_3$. Similarly to median fault plane variability $\widehat{\Psi_f}$, for each time window, we first calculated the spatial distribution of local stress tensors for each location where at least 40 focal mechanisms were available within a 10 mm distance. The input focal mechanism data were resampled and then inverted 200 times by randomly selecting either of the two nodal planes for each focal mechanism, suppressing the problem of fault plane ambiguity (e.g., Martínez-Garzón et al., 2014) in the input focal mechanism data. From this we obtained the spatial distribution of local stress tensors for a particular time window.

In the following, for each local stress tensor, we extracted the plunge of maximum principal stress $\delta_{\sigma 1}$ which is given by the eigenvector corresponding to the largest eigenvalue of the input stress tensor. Finally, we averaged maximum principal stress plunges from the whole fault surface. For plunges of $\delta_{\sigma 1} = 90°$ the local principal stresses averaged over the sample surface are aligned with the macroscopic vertical axial stress direction S_1.

The second parameter describing the local stress tensors is the tensor variability $\widehat{\Psi_{\sigma ij}}$, which was calculated with the same procedure as for the focal mechanism variability estimation. For each time window, we calculated the median out of an ensemble of rotation angles between all possible pairs of local stress tensors. Low values of $\widehat{\Psi_{\sigma ij}}$ suggest that local stress tensor orientations over the fault surface are similar.

3. Results

Here we present and describe representative time series for each of the above parameters describing the evolution of the fault system in sample WgN05. The results for samples WgN04 and WgN07 are presented in the supplementary information (Figures S5–S6 in Supporting Information S1).

3.1. AE Rates

The AE rates display a short-term (within each phase P1–P5 leading to the LSD) as well as a long-term (across whole experiment) evolution with progressive deformation of the sample (Figure 2b). The long-term evolution is characterized by an overall decrease of peak AE rates $\dot{N}$ (Figure 2b). The individual phases P1–P5 preceding LSD1-LSD5 display exponentially increasing $\dot{N}$ when approaching failure (Figure 2b). The LSD nucleation point is illuminated by a large AE event located using P-wave arrivals. Once the elevated noise from saturation of the AE system drops to background level (cf. grayed area in Figure 1e), AE aftershocks become visible, displaying a $1/t^p$ (Omori-type) decrease of AE rates typically lasting no more than about 20 s following the actual stress drop (cf. Figure S1 in Supporting Information S1). The aftershock rates then decrease with consecutive LSDs suggesting bulk smoothing of the fault surface.

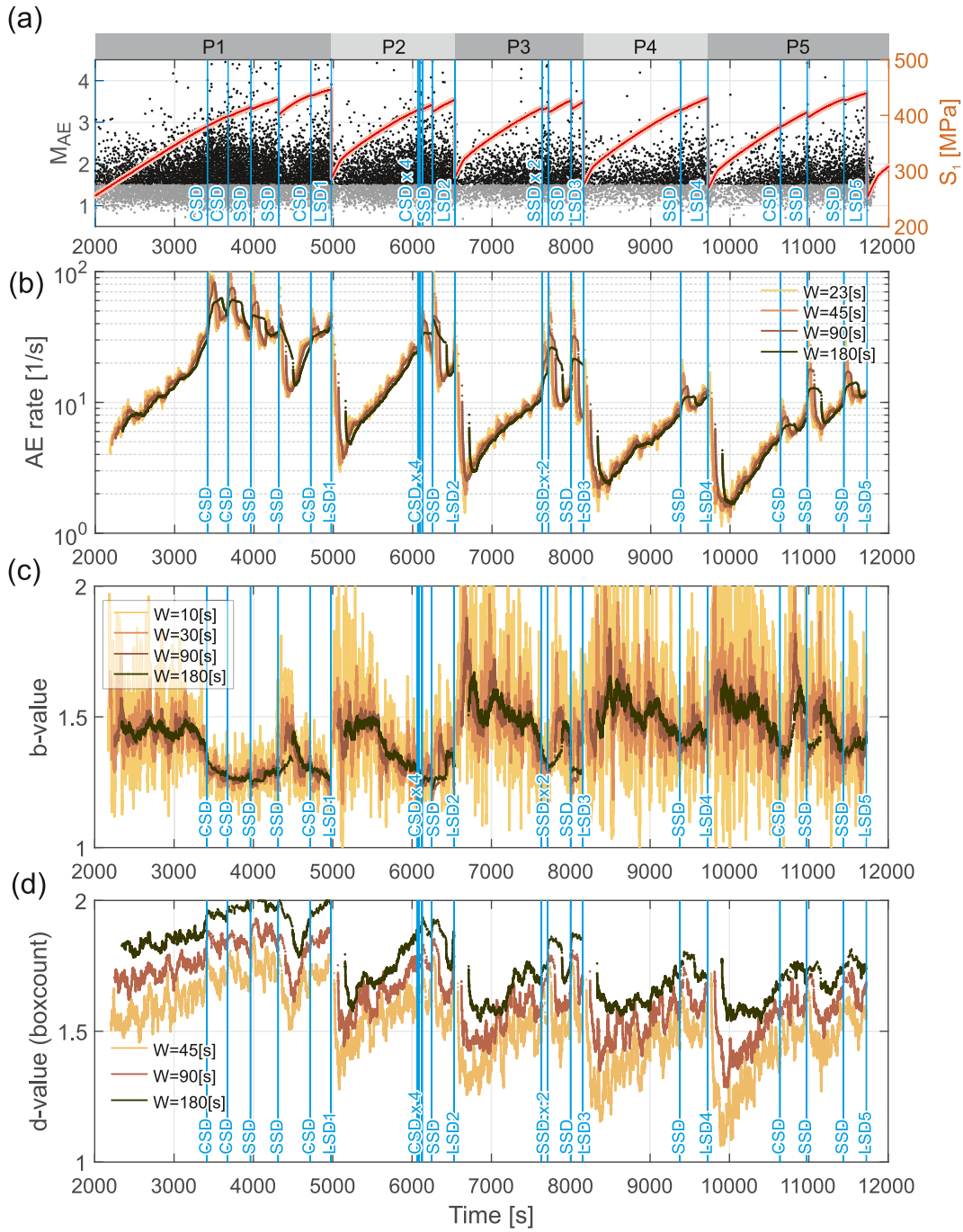

Figure 2. Temporal evolution of (b) AE event rates, (c) GR *b*-value, and (d) fractal dimension (*d*-value) from a boxcounting method calculated using different moving time windows *W [s]*. For reference, the evolution of AE magnitudes and axial stress is shown in (a).

The increase of AE rates $\dot{N}$ during each phase P1–P5 is punctuated by multiple short-lasting bursts of AE activity following SSDs and CSDs characterized by AE rates decreasing as $1/t^p$ over a short period of time (typically <10 s, Figure S1 in Supporting Information S1). All SSDs and all but one CSD show no acceleration of AE rates up to failure (cf. Figure S1 in Supporting Information S1). Only the second CSD ($T = 3672.8$ s) that occurred in phase P1 show a visible acceleration of AE rates (Figure S1b in Supporting Information S1). The SSDs and CSDs tend to reduce the overall long-term AE rates in phases preceding LSDs (Figure 1b). AE rates are closely related

to slip rate at any spatial scale (i.e., at long-scale representing the sample size and the short-scale representative of asperity size). However, there is no clear relation of peak AE rates with stress drop value.

3.2. Gutenberg-Richter *b*-Value

The temporal evolution of the *b*-value (Figure 2c) displays low *b*-values associated with CSD and SSD events (cf. Goebel et al., 2013) through all phases P1–P5, but especially during P1 and P2. This suggests that the change in *b*-value acts as a proxy generally indicating small- (cm-scale) local ruptures confined in the sample at high levels of stress. In general, a decrease in *b*-value indicates an approach to system-wide failure (LSD).

From phase P3 onwards, CSDs and SSDs are less prominent and the temporal trends of the *b*-value become somewhat more uniform and gradual. This may reflect a global conditioning process of the whole fault surface, progressive localization and overall reduction of the fault roughness at the scale of the whole sample. In P3–P5, prior to the LSDs, the *b*-values visibly decrease, and then recover to $b = 1.4$–1.6 during the initial part of the subsequent loading cycle. The amplitude of the *b*-value recovery following the LSD is likely affected by the saturation of the AE acquisition system which masks smaller aftershocks immediately following LSD, presumably reducing the jump in *b*-value in early post-slip phases. The decreasing *b*-value before some of the CSDs and SSDs typically becomes more evident if the AEs are additionally spatially constrained to those related to the activation of specific patches (see e.g. Goebel et al., 2012). Overall, the localized slips (CSDs and SSDs) tend to be preceded by a *b*-value decrease irrespective of the amplitude of macroscopic slip, thus the *b*-value is predominantly sensitive to the long-term temporal evolution (sample-wide) as well as cm-scale (asperity size) changes throughout the first phases P1–P2.

3.3. Fractal Dimension

The *d*-values derived with the boxcounting method are primarily sensitive to the spatial distribution of AEs, and less sensitive to AE density, as for example, *d*-value estimations based on the correlation integral. A *d*-value of about 2.0 corresponds to an AE hypocenter distribution across the fault surface. In contrast, *d*-values <2.0 indicate formation of distinct AE lineaments or clusters within the fault zone. The evolution of the *d*-value during individual stick-slip cycles leads to a general increase of the *d*-value ahead of each major LSD, signifying the overall increase in the AE activity across the entire fault surface as a consequence of the increased contact area between the two faces of the fault. The AE activity immediately following the LSDs is characterized by higher *d*-values that quickly decrease within the first 50–100 s following the LSD. This may be due to fault dilation associated with large slip and a destruction of small-scale asperities in contact reducing AE activity to linear or isolated clusters indicating larger asperities. As loading and shear-enhanced compaction across the fault resumes, the *d*-value increases again.

Interestingly, over stick-slip phases P1–P5 the *d*-values decrease. Local peak *d*-values are typically reached just prior to LSDs and they decrease from about 2.0 to 1.7 with consecutive LSDs. Concurrently, we observe development of a diagonal step-over (cf. Figure S7 in Supporting Information S1) that in the later phases hosts the majority of AE activity forming a quasi-linear distribution of activity and depletion in AE activity elsewhere. Our observation suggests that *d*-value is primarily sensitive to changes over the length of the whole sample, collecting information from the geometrical distribution of AE events across the whole fault surface.

3.4. Clustering Properties

The spatial distribution of AE hypocenters allows identifying transient AE clusters forming at small-scale mm-to cm-scale asperities characterizing the rough topography of the fault surfaces (Figure S7 in Supporting Information S1, see also Goebel et al., 2012, 2015). All phases P1–P5 show generally similar trends in the evolution of the median event proximity $\hat{\eta}$ parameter (Figure 3b), which signifies the level of event clustering in the combined space, time and magnitude domain. During the initial part of each stick-slip cycle at low axial stress, the median event proximity $\hat{\eta}$ is relatively large. This indicates a dominance of diffuse background activity suggesting random distribution of events in time, space and magnitude domains over the surface. This agrees with the high proportion of *mainshocks* and *singles* in the AE catalog observed during the initial portion of each stick-slip cycle (Figure 3c).

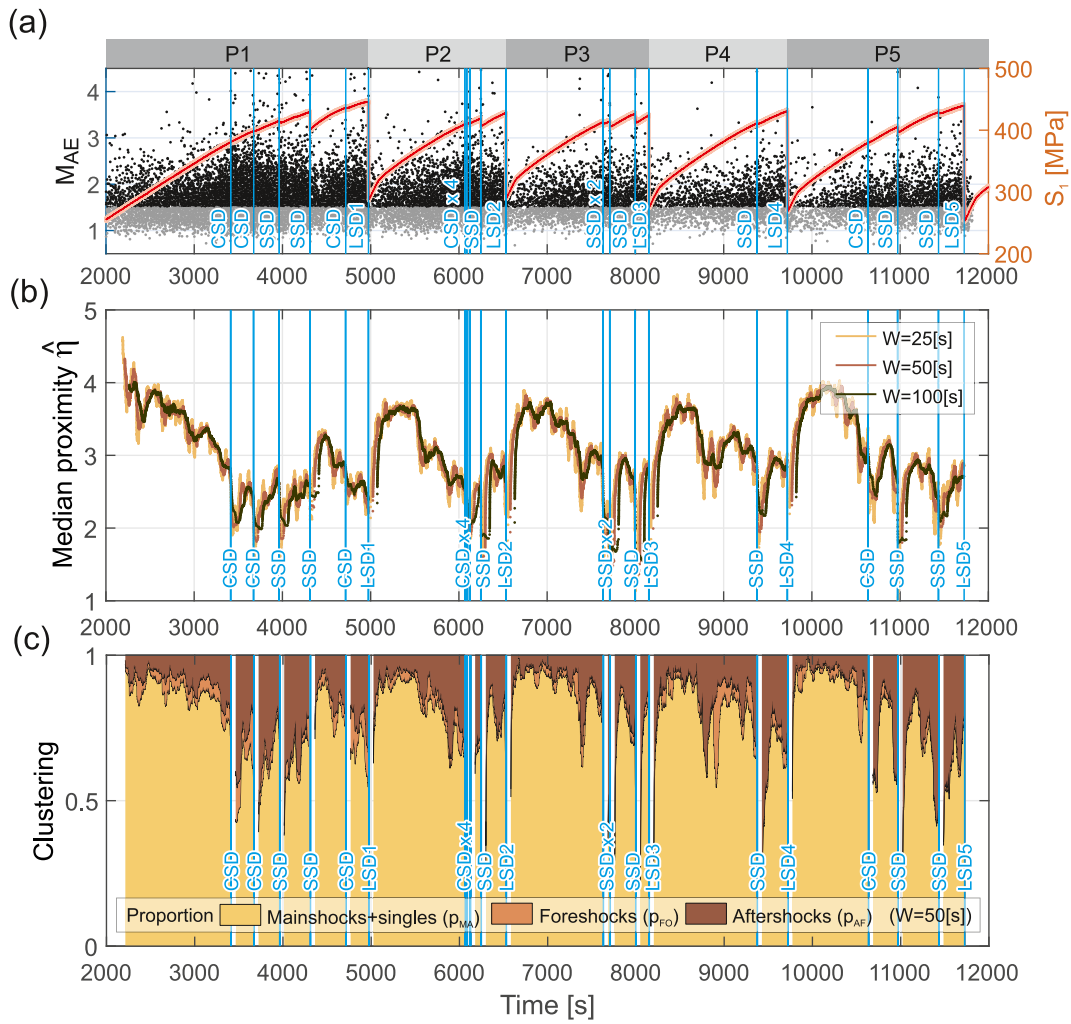

Figure 3. Temporal evolution of (a) stress and AE activity for reference, (b) Median event proximity $\hat{\eta}$ (lower $\hat{\eta}$ indicates clustering of events) and (c) proportion between AE background events (i.e., *mainshocks* and *singles*), *foreshocks* and *aftershocks* in the catalog (cf. Figure 1) as derived from clustering analysis.

With progressive loading and when approaching LSD failure, the AE rates increase and the median event proximity $\hat{\eta}$ displays a transient decrease, indicating a progressive localization of AE activity (Figure 3b). This observation is consistent with other laboratory studies (e.g., Bolton et al., 2023; Marty et al., 2023). Concurrently, we observe a decreasing proportion of *mainshocks* and *singles* that are superseded by *aftershocks* and occasionally by foreshocks (Figure 3c). The progressive localization and increasing size of AE clusters before LSD failures agree with observed patterns before several $M_W > 7$ earthquakes in Baja and southern California (Ben-Zion & Zaliapin, 2020). The proportion of foreshocks clearly does not increase ahead of the LSD, and are instead correlated with the SSD and CSD occurrence. Likewise, an increase in AEs classified as aftershocks with progressive loading ahead of the LSD appears to be linked to the more frequent occurrence of SSDs and CSDs at higher axial stresses, rather than directly with the run-up to LSD.

Some SSDs and CSDs are preceded by a visible short-term drop in the median event proximity $\hat{\eta}$ signifying increased clustering, and all CSDs and SSD display strong space-time localization within up to 20 s after the slip followed by a transient $\hat{\eta}$ recovery (Figure 3c, Figure S3 in Supporting Information S1). The amplitudes of temporal $\hat{\eta}$ changes before the CSD or SSD do not seem to correlate with the macroscopic stress drop that follows (cf. Figure S3 and Table S1 in Supporting Information S1). Accordingly, the short-lasting clustering episodes framing SSDs and CSDs are sometimes preceded by an increased proportion of AE events that are classified as *foreshocks*, especially in later loading phases. The SSDs and CSDs are always followed by an increased

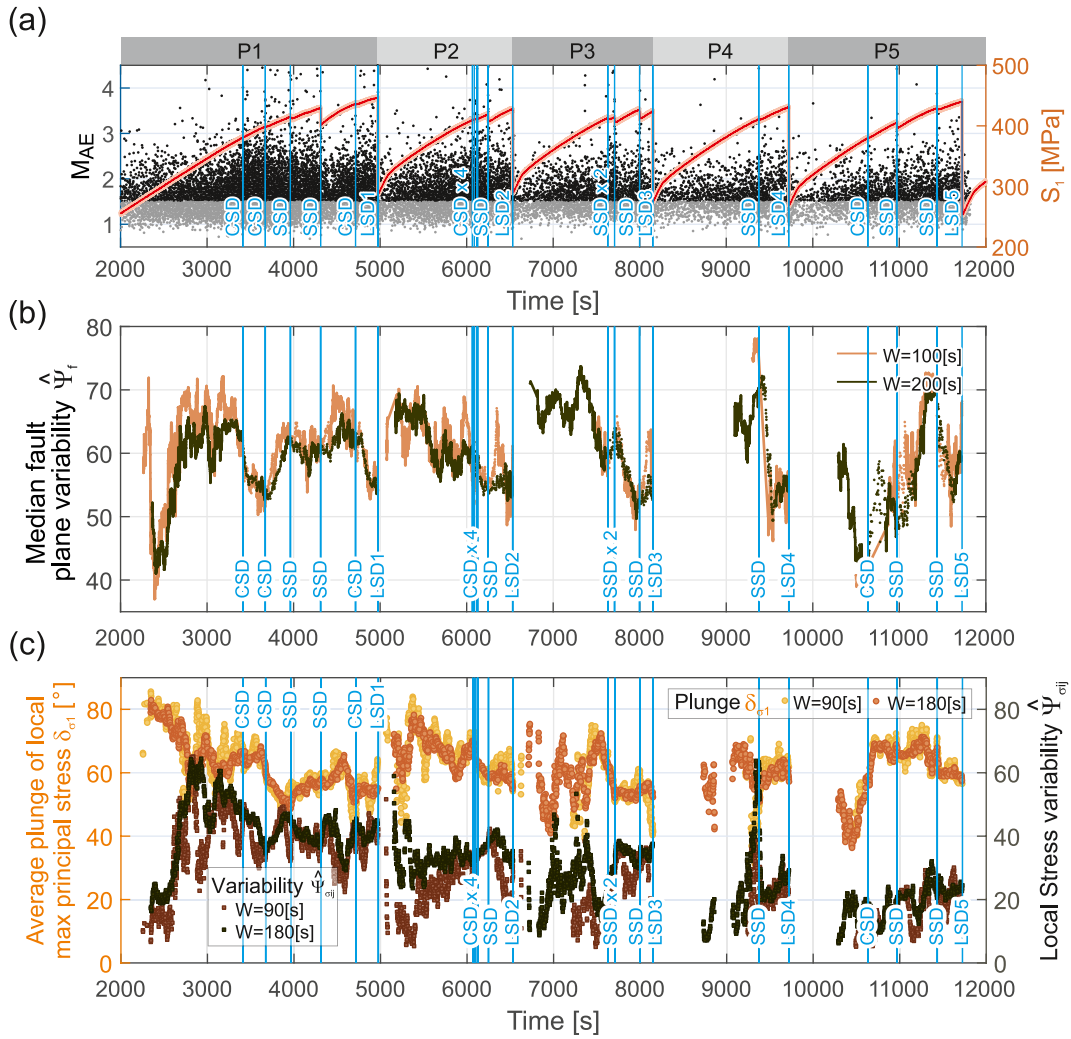

Figure 4. Temporal evolution of the (b) local fault plane variability $\widehat{\psi_f}$, (c) plunge of the local maximum stress, $\delta_{\sigma 1}$ (filled circles) and local stress tensor variability $\sigma_{Sij}(t)$ (dots). For reference, the evolution of AE magnitudes and axial stress is shown in (a) (cf. Figure 1). The visible data gaps during later phases originate from the limited amount of AE-derived MTs.

proportion of AE events classified as *aftershocks* (Figure S4 in Supporting Information S1). The proportions of *foreshocks*, *mainshocks*, and aftershocks do not substantially evolve across several stick-slip cycles, despite the fact that the number of visible SSDs and CSDs responsible for clustered seismicity seem to reduce with time (cf. Figure 3a with Figure 3c).

Time periods directly following LSDs display strong clustering with complete lack of AE *foreshocks* replaced with AEs classified as mainshocks/singles and aftershocks. The proportion of clustered to background events (e.g., Martínez-Garzón et al., 2018) seems lower on average in comparison to that in the time periods following SSD and CSD, which reflects problems with classification of events in these time periods due to the saturation of the AE system. Nevertheless, in the time period following a LSD, the initially localized AE activity progressively delocalizes within 50–100 s and the next cycle starts, initially dominated by background seismicity. In summary, the evolution of clustering properties is associated predominantly with the life cycle of cm-scale asperities (cf. Figure S7 in Supporting Information S1).

3.5. Fault Plane Variability

The observed AEs result from fracturing and frictional processes occurring on the grain scale (<mm scale). Consequently, the observed temporal evolution of fault plane variability $\widehat{\psi_f}$ (Figure 4) reflects the complex grain-

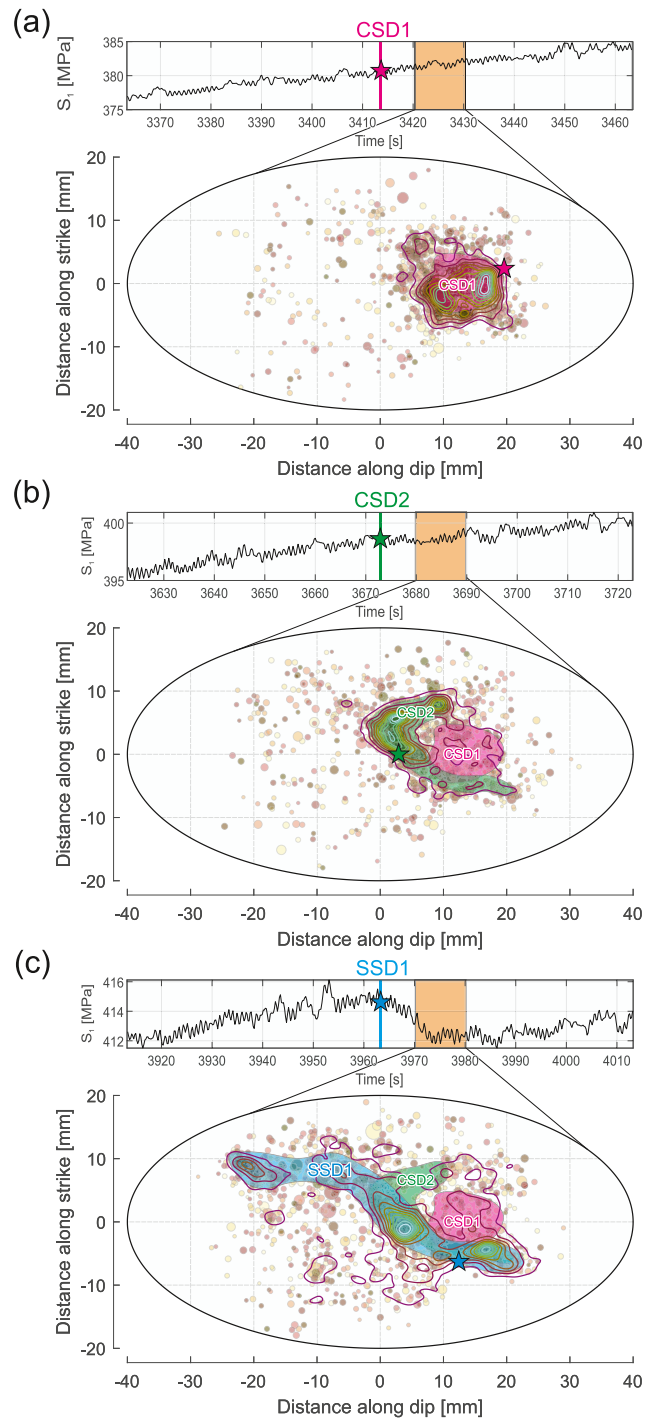

Figure 5. Surface distribution of AE activity following three slip events from the phase P1 of loading (cf. Figures 1a and 1b): (a): CSD $T = 3414$ s (cf. Figures 1c–(1f), (b): CSD $T = 3673$ s, (c): SSD $T = 3963$ s (cf. Figures 1f and 1h). In (a, b, c) filled circles show AE activity within a 10 s window starting ∼12 s following the nucleation of a slip event (star). The contour plot marks the density of events between the start of the slip event and the end of the selected time window, aggregating the damage accumulation during slip. First, two confined slips (a), (b) activate small distinct patches representing cm-length-scale asperities (magenta and green regions in all subfigures). The patches mostly do not overlap suggesting a shift in activity with subsequent slips. This suggests that failing *short-scale* asperities become inactive and 'smooth' at the cm-scales. The smoothed-out region expands ultimately to >2 cm diameter (c) giving rise to a first SSD that activates a significant part of the fault surface with AE activity accumulating in a narrow diagonal region (blue region in c). The animations presenting the damage evolution framing the occurrence of three slip events are shown in Movies S2-S4 in Supporting Information S1.

scale (mm) micromechanics. This is because the parameter compares faulting kinematics of individual AE events located close by. In general, high $\widehat{\psi_f}$ values are observed during the entire experiment, reflecting a broad orientation distribution of focal mechanisms that comprise mostly normal (parallel to fault dip) to strike-slip faulting mechanisms across the whole fault surface. During loading, fault variability mostly increases or fluctuates around a high level but, in some cases, $\widehat{\psi_f}$ decreases before LSD. The latter agrees with earlier observations of Dresen et al. (2020) and Goebel et al. (2017) indicating an increasing alignment of microslip planes ahead of LSD. However, in rough faults the process is far less prominent than observed for saw-cut faults (e.g., Goebel et al., 2017) In addition, $\widehat{\psi_f}$ seems largely unaffected by the occurrence of CSD or SSD events and does not show fundamental long-term evolution across many stick-slip phases. This suggests that the grain-scale roughness is largely preserved during the experiment.

3.6. Maximum Principal Stress Orientation and Stress Variability

Stress tensor inversion from AE-derived focal mechanisms allows inferring the local orientation of the deviatoric stress tensor and a relative measurement of its eigenvalues. Changes in principal stress orientation in response to loading, averaged over the whole fault plane, are recorded with the $\delta_{\sigma 1}$ (plunge) parameter, whereas heterogeneity of the local stress tensors is reflected in $\Psi_{\sigma ij}$ parameter.

During the initial phase P1 the plunge of the maximum principal stress orientation $\delta_{\sigma 1}$ resolved locally stays close to vertical. Subsequently, $\delta_{\sigma 1}$ progressively deviates from the vertical direction as loading increases. Ignoring some short-period outliers, local plunges of the maximum principal stress roughly vary between 90° and 40° with respect to the vertical sample axis during loading and unloading. Excluding the stick-slip cycle associated with LSD4, we find a progressive rotation of the maximum principal stress during loading while approaching remaining LSDs. This rotation is likely due to shear-enhanced compaction and build-up of shear stress during loading near the fault surface, causing a local rotation of the stress tensor. The increasing local shear stresses are released during slip events, leading to back rotation of the local stresses toward the initial stress state that is observed in early part of the phases P2–P4, following the LSD1 and LSD3, respectively. The rotation of the principal stress axes in each stick-slip cycle is associated with a slow reduction in spatial heterogeneity of the local stress, as indicated by the decreasing stress variability coefficient $\widehat{\Psi_{\sigma ij}}$.

4. Discussion

Various large earthquakes were observed to be preceded by precursory deformation and foreshock seismicity on varying scales in space and time, but the observed patterns are diverse and do not always occur (e.g., Kanamori, 1981; Kato & Ben-Zion, 2021; Kwiatek et al., 2023; Sykes, 2021; Wu et al., 2013). Recent studies of laboratory data showed that the use of AI techniques and features derived from AEs can open up new avenues toward forecasting laboratory earthquakes on *smooth* faults. However, the range of observable physical processes involved in the run-up to dynamic rupture and how they interact remain not well-understood, regardless of the scale (Ben-Zion, 2008, and references therein). Likewise, there is a need for physical understanding of the extracted data features used by AI techniques and assessment of their effectiveness in describing the run-up to failure, especially for *rough* faults (see overview in Bolton et al., 2019; Johnson et al., 2021; Karimpouli et al., 2023; Lubbers et al., 2018; Picozzi & Iaccarino, 2021).

In this paper, we employ data from laboratory experiments and use AE-derived seismo-mechanical and statistical parameters to characterize the evolution of local damage, roughness, and stress in the immediate vicinity of a rough fault surface. In particular, we investigate whether our parameters contain information on the preparation process leading to large stress drops (LSD). The sizes of AEs recorded in laboratory experiments analyzed in this study range from M_W -7 to M_W -9 (Blanke et al., 2021; Dresen et al., 2020), being at least 3 units lower than the estimated magnitude of the large stick-slips (Dresen et al., 2020). A meta-analysis by Mignan (2014) suggested that such AE activity may include key precursory information related to large laboratory earthquakes. Field observations of processes leading to large earthquakes have been categorized as pre-slip, cascade, or localization phenomena, but recent studies point toward a case-specific combination of processes (see Cattania & Segall, 2021, and reviews in McLaskey, 2019; Kato & Ben-Zion, 2021). The physically-motivated parameters used in this study are shown to (I) collectively capture the deviation from long-lasting stable deformation toward a preparatory process of large unstable failure, and (II) enable high-resolution monitoring of local damage,

roughness, and stress at different temporal and length scales. This allows us to identify the time in which the fault enters a critical stage during which a system-size dynamic rupture may seemingly occur at any time.

The stick-slip experiments are performed on a naturally fractured rock sample (Goebel et al., 2014, 2015). The fault surface (e.g., Figure S7 for WgN05 in Supporting Information S1) displays high initial roughness representing a strongly segmented and juvenile fault in nature. This is in contrast to a smooth saw-cut surfaces which may be more representative of a fault with large displacement (cf. Goebel et al., 2017). As in many past experiments (see e.g. Harbord et al., 2017), slip events on a rough fault show a rich mechanical behavior. The large (LSD) and small (SSD) macroscopic slips of the whole or significant portions of the surface display varying durations and amplitudes reflecting fast and slow slip velocities as well as large and small stress drops (cf. Table S1 in Supporting Information S1). Smaller slips confined within the fault surface (CSD) are highlighted solely by AE activity, but not with external readings. In consequence, the seismo-mechanical behavior generally shows much stronger or fractal-like fluctuations compared to saw-cut faults in triaxial stick-slip experiments (cf. Goebel et al., 2015, 2017), and double-direct shear experiments containing gouge (e.g., Bolton et al., 2021; Scuderi et al., 2017). This highlights the need for a careful extraction of meaningful features/parameters from AE data describing the processes leading to system-size failure to enrich information on preparatory processes.

4.1. Fault Roughness, Damage and Stress Evolution

The complex evolution of fault damage, roughness and stress across multiple stick-slip cycles with progressive shearing is related to *grain-scale* comminution, gouge production and destruction of *small-scale* asperities that ultimately lead to generation of the persisting *large-scale* topography (cf. Goebel et al., 2012, 2015, 2017; Kwiatek, Goebel, & Dresen, 2014). Development of roughness at these different spatial scales has always some AE response (cf. Goebel et al., 2014). The length scale of the roughness/damage evolution processes may be captured with AE source parameters via their collective seismo-mechanical and statistical proxies (cf. Blanke et al., 2021; Dresen et al., 2020). In this study, grain-scale roughness behavior is represented by the fault plane variability, which captures the difference between focal mechanisms of neighboring events. The *small-scale* roughness evolution of small cm-scale asperities is observed with collective properties of AE activity such as event rates, and predominantly with (spatio-)temporal features including clustering and local stress field orientation and local stress variability. Finally, the development of the *large-scale* (>cm) topography is captured by long-term trends in the temporal evolution of global properties including *d*-value, *b*-value and event rates $\dot{N}$.

The complex long-term (across many stick-slip cycles) evolution of fault roughness is primarily documented in the spatio-temporal AE distribution (*d*-value) and localized damage indicators (*b*-value, AE rate, cf. Figure 2), as presented in past studies (Dresen et al., 2020; Goebel et al., 2013, 2017; Kwiatek, Goebel, & Dresen, 2014). A decrease in local stress variability (Figure 4c), the new parameter calculated using AE stress tensor inversion, confirms progressive smoothing of the large-scale fault surface. These parameters signify that fault roughness evolves substantially up to LSD2 but less in P3–P5. This is likely because after multiple slip events, small-scale asperities are progressively destroyed but a *large-scale* fault topography remains, as revealed by the post-mortem inspection of deformed samples (Figure S7 in Supporting Information S1). Consequently, the later P3–P5 AE activity is focused on these larger asperities at the expense of a more uniform distribution on the fault. This results in a general *d*-value decrease across many stick-slip cycles converging toward $d = 1.6$ close to the peak stresses for the last cycles.

The AE rate and *d*-value evolution toward higher values in each phase preceding LSD imply spreading of AE events across the fault (Figure 2d) imposed by enhanced contact area between the granular material forming the fault zone at elevated normal load (Dieterich & Kilgore, 1996) (cf. Movie S1 in Supporting Information S1). This is associated with a general *b*-value decrease within the stick-slip cycle, interpreted as a signature of increased stress (Goebel et al., 2013; Schorlemmer et al., 2005) or damage accumulation (e.g., Main, 1991). Anti-correlations of *b*- and *d*-values, as observed in our study, have been reported in similar experiments (Main, 1991, 1992). However, the *d*-values and *b*-values are also frequently linearly related through $D = 2b$ (Aki, 1981; King, 1983) as found in some studies of natural earthquakes (Wyss et al., 2004) and other laboratory experiments (e.g., Goebel et al., 2017). It is therefore conceivable that interpretation of *b*- and *d*-value correlations and trends should be considered case-dependent (see also Legrand, 2002) and sensitive to the methodology used. The evolution of the used parameters within one cycle toward the LSD is superposed with high-frequency

variations. These originate from activation of *short-scale* asperities at high levels of axial stress, visible as CSD and SSD events and associated transient clusters of AEs (cf. Movie S1–S4 in Supporting Information S1).

Post-mortem surface observations suggest that *small-scale* asperities causing clustered AE activity have been progressively erased (cf. Goebel et al., 2012, 2015) but *grain-scale* roughness remained unchanged. The former is supported by general decrease of the local stress variability (*small-scale*) over several slips (Figure 4c), although we do not observe significant evolution of the fault plane variability that is governed by *grain-scale* fracturing. High values of fault plane variability observed during the whole experiment, especially if compared with saw-cut faults (cf. Dresen et al., 2020), reflect complex, inter-granular processes related to shear-enhanced compaction of the granular material forming the fault zone (Kwiatek, Goebel, & Dresen, 2014). This indicates persistence of *grain-scale* sub-mm roughness of the stress field. The micromechanical *grain-scale* roughness evolution leads effectively to smoothing of the short-scale asperities, and the short-scale stress field, as indicated by the decreasing local stress variability.

Beyond P2 we note that fewer and smaller SSDs occur prior to LSDs. Our observations suggest that with progressive slip and smoothing of small-*scale* fault heterogeneities, the stress field across the whole fault surface becomes more uniform, as the length scale of large heterogeneities becomes more prominent. Increased contact area, and smoothing of the *small-scale* asperities responsible for local stress concentrations result in *large-scale* homogenization of the stress field while approaching the LSD. This agrees with findings from numerical modeling (Ben-Zion et al., 2003) as discussed further in the next section.

To summarize, we find that *grain-scale* (<mm) and *large-scale* (>cm) roughness remain largely unchanged across many slip events in contrast to the *small-scale* (mm-to-cm) roughness involving asperities distributed initially across the surface that are progressively erased with repeating slips.

4.2. Multi-Scale Preparatory Process and Intermittent Criticality

Within single stick-slip cycles, the evolving space-time-magnitude correlation η_j of AEs indicates formation of distinct clusters (Figure 3b). Together with progressive *b*-value decrease and increased event rates, the combined parameter evolution implies accelerating deformation and localization ahead of the LSDs, in agreement with observations from lab tests and field data across different scales (Das & Scholz, 1981; see e.g., Ben-Zion & Zaliapin, 2020; Lei & Ma, 2014; McBeck et al., 2022). Moreover, the exponentially increasing AE rates indicate accelerated seismic release (ASR), which is a non-universal earthquake precursory behavior (e.g., Ben-Zion & Lyakhovsky, 2002; Bufe et al., 1994; Mignan, 2011). However, the discussed set of parameters does not unequivocally signify the proximity to system-size events (LSDs), as similar trends are observable at smaller spatio-temporal scales before individual SSDs or even CSDs.

At about 85%–90% of the maximum axial stress (i.e., hundreds of seconds before LSD, corresponding to the yield stress of the fault), the examined parameters tend to mostly fluctuate around a saturation level with occurrence of SSDs and CSDs. Such saturation level is already observed in the first cycle P1 starting with the first CSD (ca. 1,500 s before the LSD1) at about 85% peak stress and 75% of failure time t_f. In addition, we observe that the length of the saturation period prior to failure shortens with each stick-slip cycle, suggesting that the duration over which stress and seismic parameters fluctuate depends on the temporal evolution of fault roughness and associated stress heterogeneity. At the saturation level, *b*-values and $\hat{\eta}$ remain mostly low as both tend to drop significantly in the last part of the loading cycle. Likewise, the clustered AE activity including AE foreshock-mainshock-aftershock sequences increases, resulting in a reduced proportion of background events (Figure 3c). Clustered AE activity clearly associated with SSDs and CSDs typically consists of aftershocks and few foreshocks framing the mainshock, suggesting active stress interaction between events as stress transfer occurs across mm-to cm-length scales of the stress field associated with asperities (see next section).

The externally measured axial stress S_1 fluctuates around a critical state between ~85% and peak stress. This has been described previously as intermittent criticality and was observed in nature and numerical models in combination with accelerated seismic release and decreasing *b*-value (cf. Ben-Zion et al., 2003; Bowman & Sammis, 2004). In particular, Ben-Zion et al. (2003) showed in simulations of stress and seismicity on a large heterogeneous fault that toward the end of a seismic cycle, a critical (fractal-like) disorder of the stress field heterogeneity is reached over a broad range of scales. This is found in a representative model for the brittle crust

(model F, see Ben-Zion et al., 2003), which is characterized by realistic dynamic weakening. In agreement with our results, any stress perturbation at a high stress level may trigger a small or system wide seismic event. The ultimate size of the event is conditioned on whether the stress level is sufficiently high over a large portion of the fault surface and smooth over this length scale, allowing the event to propagate. Other models of nucleation of large events on rough faults were proposed using, for example, models of progressive depinning of local asperities collectively reaching the critical nucleation length (Lebihain et al., 2021) and partitioning of seismic and aseismic slip and their collective influence on asperities failure and ultimate nucleation (e.g., Cattania & Segall, 2021).

Following Ben-Zion et al. (2003), large-scale correlation of elevated stresses enables the generation of large events over a smoothed portion of the stress field. However, the nucleation of such instability remains a statistical event, as it can be in principle triggered by a *small-scale* or even a *grain-scale* stress perturbation at the right location. The statistical fluctuations before triggering of large lab earthquakes involve CSD and SSD events. These events lead to local stress relaxation across limited portions of the fault and stress transfer to the surrounding regions (Figure 5). The concentrated stress transfer near previous failure events is evidenced by significant clustering of AE activity forming foreshocks and aftershock sequences at high axial stresses once CSDs and SSDs become more frequent. The redistribution of stress and the stress drops due to CSDs and SSDs may cause the fault to temporarily retreat from the critical stress level. As loading continues, stress recovers and long-range stress correlations are reestablished leading eventually to a system size (LSD) event.

4.3. Earthquake Interaction on Different Length Scales

At the beginning of a stick slip cycle, distributed background activity represents >90% of the total AE activity (Figure 3c). As loading increases, activity rates increase, background activity and *b*-values decrease and there is a progressive spatio-temporal localization of AE events approaching LSDs (Figure 3b). This is accompanied by increasing slip along the fault. The observed evolution of event proximity and mainshock aftershock distribution may signal AEs triggering close to larger slip events.

Compared to smooth saw-cut faults where shear strain is localized and off-fault damage is minor, increasing fault roughness results in significant off-fault damage and a relatively broad damage zone (Goebel et al., 2017). As a result, shear strain is less localized compared to smooth faults and fault slip starts at lower shear stress. Therefore, precursory slip displays a larger fraction of aseismic deformation compared to smooth faults that unlock only at significantly higher stresses (e.g., Dresen et al., 2020). For rough faults, the increase in shear stress, compaction and contact area of the fault surfaces results in activation of a growing number of asperities leading to CSDs and LSDs. High local stress concentrations ahead of CSDs and SSDs, as well as local stress redistribution following these events, produces observable event clustering/triggering (see e.g. Davidsen et al., 2017, 2021; Martínez-Garzón et al., 2018; Schoenball et al., 2012). In agreement with Davidsen et al. (2017, 2021), the local stress concentrations produce AE event interactions. This highlights the importance of local stress intensities that control the evolution of the investigated parameters and the role of inter-event triggering (Davidsen et al., 2017; Meredith & Atkinson, 1983).

AE aftershocks following LSDs are controlled by residual elastic strain energy, and also depend on differences in fault roughness and slip stability (Goebel et al., 2023). However, aftershocks are relatively scarce in the examined data with respect to those framing SSDs and CSDs. This is partially because very early AE aftershocks following LSD or SSD are masked by the saturation of the AE system with continuous noise consisting of abundant overlapping AEs lasting up to 100 ms (see Table S1 in Supporting Information S1). However, for LSDs the entire fault blocks are displaced and strength across the interface is reduced to sliding friction. Since the LSD rupture reaches the sample size, no stress redistribution beyond the rupture periphery is possible, which is in contrast to the confined or some small-scale (SSD) ruptures where the stress is redistributed internally. This is visibly reducing the aftershock productivity after LSDs, as the stress associated with large rupture is effectively unloaded in the triaxial machine. This difference in behavior of LSD and SSD/CSD in terms of stress transfer poses some challenges for the analysis of aftershocks following LSD/SSD and CSD. This observation needs to be considered while training models forecasting the time-to-failure of laboratory tests. However, Karimpouli et al. (2023) showed that training machine learning models forecasting time-to-failure using carefully framed data is possible, and the effects of boundary conditions can be minimized.

5. Potential Applications to Earthquake Forecasting

Many studies attempted to characterize precursory deformation preceding large earthquakes using changes in seismicity rate, accelerated release of seismic moment and energy, changes of *b*-values, and other parameters calculated from geodetic and seismic data along with other measurements (e.g., Acosta et al., 2019; Bentz et al., 2019; Bolton et al., 2021; Bowman et al., 1998; Gulia et al., 2016; Picozzi & Iaccarino, 2021; Shreedharan et al., 2021; Varnes, 1989). However, very few if any datasets on the field scale have enough resolution to allow tracking evolution of the parameters discussed in our study during the preparatory phase for large events. This gap may be reduced using modern AI techniques that allow enhancing seismic catalogs (e.g., Mousavi & Beroza, 2022; Trugman & Ross, 2019). This will provide new information on processes preceding large earthquakes via, for example, additional informative foreshocks (Mignan, 2014). Meanwhile, at the laboratory scale, parameters calculated from continuous waveform data or event catalogs have been used already to successfully forecast the evolution of shear stress, friction, or time-to-failure (see e.g., Lubbers et al., 2018; McBeck et al., 2020, Johnson et al., 2021, and references therein). It is important to note that the seismo-mechanical behavior of *smooth* laboratory faults differs from that observed for *rough* faults. The former tends to display a simpler and repetitive behavior, which is attributed to the homogeneity of the fault gouge layer (e.g., Johnson et al., 2021; Lubbers et al., 2018) or structural simplicity of the fault surface (e.g., Goebel et al., 2017; Kwiatek, Goebel, & Dresen, 2014). Smooth faults also display clearly identifiable transitions from quasi stable deformation toward rapid acceleration resulting in seismic slip. This is associated with a non-linear accelerating seismic response, and considerably simplifies the training of ML algorithms. Even for such repetitive stick-slip experiments on saw-cuts, it was found that fault gouge layers evolve during the experiments reducing the time-to-failure forecasting quality (see discussion in Johnson et al., 2021).

Comparisons of past laboratory tests on saw-cut faults and rough faults including results from this study highlight the crucial impact of fault structural heterogeneity or fault roughness, related stress field heterogeneity, stress transfer, and their temporal, spatial and length-scale evolution on our capability of forecasting large failure events. Faults evolve with progressive loading over geological timescales, displaying a qualitatively comparable evolution of many parameters (e.g., localization, *b*-value) regardless of their structural and mechanical complexity (Ben-Zion & Sammis, 2003; Tchalenko, 1970). However, it is feasible to observe very different precursory signatures, depending on fault structure (roughness, complexity) and other conditions (Ellsworth & Bulut, 2018; Huang et al., 2020; Kato & Ben-Zion, 2021; Kwiatek et al., 2023). For rough faults, our study suggests that a combination of physics-based parameters, reinforced with ML techniques, can indicate when the system is entering a critical stage. However, identifying the final stage immediately preceding system-size earthquakes may not be possible in the intermittent criticality framework and ultimately conditioned by the finite spatiotemporal resolution of the monitoring capabilities. Additional parameters yet to be developed may allow a closer identification of the final triggering of large events. In any case, the ability to forecast large natural earthquakes will benefit from dense instrumentation around hazardous faults that provide higher resolution data (e.g., Ben-Zion et al., 2022).

Based on our experimental observations, Karimpouli et al. (2023) found that the derived parameter pool characterizing different aspects of AE event organization in space and time, damage, stress and roughness evolution, enabled developing and constraining multi-parameter models of time-to-failure forecasting for complex rough laboratory faults. This may be done even with a considerably lower amount of input data compared to the saw-cut faults. In addition, Karimpouli et al. (2023) emphasize the importance of the new features characterizing local stress evolution derived from seismic moment tensors and stress tensor inversion of AEs in time-to-failure forecasting. Interestingly, their analysis highlights that the parameters are collectively important for the accuracy of time-to-failure prediction, but need not necessarily be correlated individually with time to failure. In other words, the developed neural networks benefit from utilization of seemingly unimportant, yet novel details supplied by some parameters to improve the ultimate prediction. Using unsupervised K-means clustering of the seismo-mechanical and statistical parameters developed here, Karimpouli et al. (2024) showed that it is possible to automatically identify a transition from stable deformation to an intermittent criticality state, with the most significant parameters being clustering properties using the decomposition of Zaliapin and Ben-Zion (2013a, b) as well as seismicity rates. They observed that the developed unsupervised scheme is able to recognize even finer transient processes related to the activation of smaller asperities, and depicted with scaled-down versions of CSDs composed of even shorter and spatially more confined clusters of AEs. These machine-learning enhanced findings are important in the context of the intermittent criticality model of Ben-Zion et al. (2003) shown here to

provide a framework that can help to explain our results. As the final large slip may be triggered by a very small stress perturbation at the right location, this would suggest that improving the forecasting of large events requires zooming-in further into the clustering processes of CSDs and searching for potential deviation from their behavior ahead of the main rupture.

6. Conclusions

We studied the preparatory processes preceding laboratory earthquakes on rough faults using an ensemble of 10 seismo-mechanical and statistical features. These physics-based parameters describe damage and stress evolution in the fault zone, localization processes, local micromechanics and earthquake interactions, as well as local stress field evolution and stress field heterogeneity.

The selected features enable understanding a diversity of processes occurring at different spatial and temporal scales during the preparatory phase preceding system-size laboratory earthquakes, these features can help constraining the input for multi-parameter AI-aided models of earthquake forecasting.

The developed set of precursory parameters highlights localization processes preparing system-size earthquakes. However, the parameters are sensitive to length scales of fault surface roughness and associated roughness of the stress field, both rapidly evolving in the course of an experiment. The spatio-temporal evolution of fault surface and stress roughness poses limitations on our ability to monitor and forecast the run-up to large laboratory earthquakes.

We identify a transition from stable deformation to an intermittent criticality state allowing the occurrence of large events. This stage is characterized by abundant AE activity highlighting persistent heterogeneity of the stress field at the sub-mm grain-scale. Spatio-temporal AE activity bursts indicate small confined slips in the sample marking a progressive breakdown of asperities. These confined slips superimpose and interact, collectively preparing the fault surface for a system-size slip by progressive smoothing the short- (mm-to-cm) scale stress field. Ultimately, the development of large-scale correlation of elevated stresses enables the propagation of a large slip event over the smoothed portion of the fault, triggered even by a minor stress perturbation.

A system-size earthquake occurring at a state of intermittent criticality is a statistical event that cannot be predicted deterministically. However, using a combination of the parameters described in this study allows identifying the onset time when a fault enters a critical stage. This may be improved with AI classification techniques using cross-scale, physics-based parameters to detect the critical state of a fault system.

Data Availability Statement

Seismic catalogs, moment tensor catalogs, raw waveform data, geomechanical data and associated information related to stick-slip experiments analyzed in this study are available at GFZ Data Services via separate data publication (CC-BY 4.0 license): Kwiatek and Goebel (2024).

Acknowledgments

We would like to thank G.C. Beroza, J. Davidsen, T. Weigel, D. Cas, H. Grover and B. Orlecka-Sikora for useful discussions during preparation of the manuscript. We acknowledge B. Fryer and two Anonymous Reviewers for valuable comments. The study was supported by the GeoForschungsZentrum Potsdam. The work of YBZ on analysis and interpretation was supported by the U. S. Department of Energy (Award DE-SC0016520). P.M.G acknowledges funding from the Helmholtz Young Investigators Group VH-NG-1232 (SAIDAN) and ERC Starting Grant −101076119 (QUAKEHUNTER). Open Access funding enabled and organized by Projekt DEAL.

References

Acosta, M., Passelègue, F. X., Schubnel, A., Madariaga, R., & Violay, M. (2019). Can precursory moment release scale with earthquake magnitude? A view from the laboratory. *Geophysical Research Letters*, *46*(22), 12927–12937. https://doi.org/10.1029/2019GL084744

Aki, K. (1981). A probabilistic synthesis of precursory phenomeena. *Earthquake Prediction*, 566–574. https://doi.org/10.1029/ME004p0566

Baiesi, M., & Paczuski, M. (2004). Scale-free networks of earthquakes and aftershocks. *Physical Review E - Statistical Physics, Plasmas, Fluids, and Related Interdisciplinary Topics*, *69*(6), 066106. https://doi.org/10.1103/PhysRevE.69.066106

Bakun, W. H., Aagaard, B., Dost, B., Ellsworth, W. L., Hardebeck, J. L., Harris, R. A., et al. (2005). Implications for prediction and hazard assessment from the 2004 Parkfield earthquake. *Nature*, *437*(7061), 969–974. https://doi.org/10.1038/nature04067

Bentz, S., Martínez-Garzón, P., Kwiatek, G., Dresen, G., & Bohnhoff, M. (2019). Analysis of microseismicity framing ML > 2.5 earthquakes at the geysers geothermal field, California. *Journal of Geophysical Research: Solid Earth*, *124*(8), 8823–8843. https://doi.org/10.1029/2019JB017716

Ben-Zion, Y. (2008). Collective behavior of earthquakes and faults: Continuum-discrete transitions, evolutionary changes and corresponding dynamic regimes. *Review of Geophysics*, *46*(4), RG4006. https://doi.org/10.1029/2008RG000260

Ben-Zion, Y., Beroza, G., Bohnhoff, M., Gabriel, A.-A., & Mai, P. M. (2022). A grand challenge international infrastructure for earthquake science. *Seismological Research Letters*, *93*(6), 2967–2968. https://doi.org/10.1785/0220220266

Ben-Zion, Y., Eneva, M., & Liu, Y. (2003). Large earthquake cycles and intermittent criticality on heterogeneous faults due to evolving stress and seismicity. *Journal of Geophysical Research: Solid Earth*, *108*(B6). https://doi.org/10.1029/2002JB002121

Ben-Zion, Y., & Lyakhovsky, V. (2002). Accelerated seismic release and related aspects of seismicity patterns on earthquake faults. *Pure and Applied Geophysics*, *159*(10), 2385–2412. https://doi.org/10.1007/s00024-002-8740-9

Ben-Zion, Y., & Rice, J. R. (1997). Dynamic simulations of slip on a smooth fault in an elastic solid. *Journal of Geophysical Research*, *102*(B8), 17771–17784. https://doi.org/10.1029/97JB01341

Ben-Zion, Y., & Sammis, C. G. (2003). Characterization of fault zones. *Pure and Applied Geophysics*, *160*(3–4), 677–715. https://doi.org/10.1007/PL00012554

Ben-Zion, Y., & Zaliapin, I. (2020). Localization and coalescence of seismicity before large earthquakes. *Geophysical Journal International*, *223*(1), 561–583. https://doi.org/10.1093/gji/ggaa315

Blanke, A., Kwiatek, G., Goebel, T. H. W., Bohnhoff, M., & Dresen, G. (2021). Stress drop–magnitude dependence of acoustic emissions during laboratory stick-slip. *Geophysical Journal International*, *224*(2), 1371–1380. https://doi.org/10.1093/gji/ggaa524

Bolton, D. C., Marone, C., Saffer, D., & Trugman, D. T. (2023). Foreshock properties illuminate nucleation processes of slow and fast laboratory earthquakes. *Nature Communications*, *14*(1), 3859. https://doi.org/10.1038/s41467-023-39399-0

Bolton, D. C., Marone, C., Shokouhi, P., Rivière, J., Rouet-Leduc, B., Hulbert, C., & Johnson, P. A. (2019). Characterizing acoustic signals and searching for precursors during the laboratory seismic cycle using unsupervised machine learning. *Seismological Research Letters*, *90*(3), 1088–1098. https://doi.org/10.1785/0220180367

Bolton, D. C., Shreedharan, S., Rivière, J., & Marone, C. (2021). Frequency-magnitude statistics of laboratory foreshocks vary with shear velocity, fault slip rate, and shear stress. *Journal of Geophysical Research: Solid Earth*, *126*(11), e2021JB022175. https://doi.org/10.1029/2021JB022175

Bouchon, M., Durand, V., Marsan, D., Karabulut, H., & Schmittbuhl, J. (2013). The long precursory phase of most large interplate earthquakes. *Nature Geoscience*, *6*(4), 299–302. https://doi.org/10.1038/ngeo1770

Bowman, D. D., Ouillon, G., Sammis, C. G., Sornette, A., & Sornette, D. (1998). An observational test of the critical earthquake concept. *Journal of Geophysical Research: Solid Earth*, *103*(B10), 24359–24372. https://doi.org/10.1029/98JB00792

Bowman, D. D., & Sammis, C. G. (2004). Intermittent criticality and the gutenberg-richter distribution. *Pure and Applied Geophysics*, *161*(9), 1945–1956. https://doi.org/10.1007/s00024-004-2541-z

Bufe, C. G., Nishenko, S. P., & Varnes, D. J. (1994). Seismicity trends and potential for large earthquakes in the Alaska-Aleutian region. *Pure and Applied Geophysics*, *142*(1), 83–99. https://doi.org/10.1007/BF00875969

Cattania, C., & Segall, P. (2021). Precursory slow slip and foreshocks on rough faults. *Journal of Geophysical Research: Solid Earth*, *126*(4), e2020JB020430. https://doi.org/10.1029/2020JB020430

Corbi, F., Sandri, L., Bedford, J., Funiciello, F., Brizzi, S., Rosenau, M., & Lallemand, S. (2019). Machine learning can predict the timing and size of analog earthquakes. *Geophysical Research Letters*, *46*(3), 1303–1311. https://doi.org/10.1029/2018GL081251

Das, S., & Scholz, C. H. (1981). Theory of time-dependent rupture in the Earth. *Journal of Geophysical Research: Solid Earth*, *86*(B7), 6039–6051. https://doi.org/10.1029/JB086iB07p06039

Davidsen, J., Goebel, T., Kwiatek, G., Stanchits, S., Baró, J., & Dresen, G. (2021). What controls the presence and characteristics of aftershocks in rock fracture in the lab? *Journal of Geophysical Research: Solid Earth*, *126*(10), e2021JB022539. https://doi.org/10.1029/2021JB022539

Davidsen, J., Kwiatek, G., Charalampidou, E.-M., Goebel, T. H. W., Stanchits, S., Rueck, M., & Dresen, G. (2017). Triggering processes in rock fracture. *Physical Review Letters*, *119*(6), 068501. https://doi.org/10.1103/PhysRevLett.119.068501

De Geus, T. W. J., Popović, M., Ji, W., Rosso, A., & Wyart, M. (2019). How collective asperity detachments nucleate slip at frictional interfaces. *Proceedings of National Academy of Science*, *116*(48), 23977–23983. https://doi.org/10.1073/pnas.1906551116

Dieterich, J. H. (1978). Preseismic fault slip and earthquake prediction. *Journal of Geophysical Research*, *83*(B8), 3940–3948. https://doi.org/10.1029/JB083iB08p03940

Dieterich, J. H., & Kilgore, B. (1996). Implications of fault constitutive properties for earthquake prediction. *Proceedings of National Academy of Science*, *93*(9), 3787–3794. https://doi.org/10.1073/pnas.93.9.3787

Dresen, G., Kwiatek, G., Goebel, T., & Ben-Zion, Y. (2020). Seismic and aseismic preparatory processes before large stick–slip failure. *Pure and Applied Geophysics*, *177*(12), 5741–5760. https://doi.org/10.1007/s00024-020-02605-x

Durand, V., Bentz, S., Kwiatek, G., Dresen, G., Wollin, C., Heidbach, O., et al. (2020). A two-scale preparation phase preceded an Mw 5.8 earthquake in the Sea of Marmara offshore Istanbul, Turkey. *Seismological Research Letters*, *91*(6), 3139–3147. https://doi.org/10.1785/0220200110

Ellsworth, W. L., & Beroza, G. C. (1995). Seismic evidence for an earthquake nucleation phase. *Science*, *268*(5212), 851–855. https://doi.org/10.1126/science.268.5212.851

Ellsworth, W. L., & Bulut, F. (2018). Nucleation of the 1999 Izmit earthquake by a triggered cascade of foreshocks. *Nature Geoscience*, *11*(7), 531–535. https://doi.org/10.1038/s41561-018-0145-1

Geller, R. J., Jackson, D. D., Kagan, Y. Y., & Mulargia, F. (1997). Earthquakes cannot be predicted. *Science*, *275*(5306), 1616. https://doi.org/10.1126/science.275.5306.1616

Goebel, T. H. W., Becker, T. W., Schorlemmer, D., Stanchits, S., Sammis, C., Rybacki, E., & Dresen, G. (2012). Identifying fault heterogeneity through mapping spatial anomalies in acoustic emission statistics. *Journal of Geophysical Research: Solid Earth*, *117*(B3). https://doi.org/10.1029/2011JB008763

Goebel, T. H. W., Brodsky, E. E., & Dresen, G. (2023). Fault roughness promotes earthquake-like aftershock clustering in the lab. *Geophysical Research Letters*, *50*(8), e2022GL101241. https://doi.org/10.1029/2022GL101241

Goebel, T. H. W., Kwiatek, G., Becker, T. W., Brodsky, E. E., & Dresen, G. (2017). What allows seismic events to grow big? Insights from b-value and fault roughness analysis in laboratory stick-slip experiments. *Geology*, *45*(9), 815–818. https://doi.org/10.1130/G39147.1

Goebel, T. H. W., Sammis, C. G., Becker, T. W., Dresen, G., & Schorlemmer, D. (2015). A comparison of seismicity characteristics and fault structure between stick–slip experiments and nature. *Pure and Applied Geophysics*, *172*(8), 2247–2264. https://doi.org/10.1007/s00024-013-0713-7

Goebel, T. H. W., Sammis, C. G., Dresen, G., & Schorlemmer, D. (2014). Off-fault damage and acoustic emission distributions during the evolution of structurally-complex faults over series of stick-slip events. *Geophysical Journal International*, *197*(3), 1705–1718. https://doi.org/10.1093/gji/ggu074

Goebel, T. H. W., Schorlemmer, D., Becker, T. W., Dresen, G., & Sammis, C. G. (2013). Acoustic emissions document stress changes over many seismic cycles in stick-slip experiments. *Geophysical Research Letters*, *40*(10), 2049–2054. https://doi.org/10.1002/grl.50507

Goodfellow, S. D., & Young, R. P. (2014). A laboratory acoustic emission experiment under in situ conditions. *Geophysical Research Letters*, *41*(10), 3422–3430. https://doi.org/10.1002/2014GL059965

Gounon, A., Latour, S., Letort, J., & El Arem, S. (2022). Rupture nucleation on a periodically heterogeneous interface. *Geophysical Research Letters*, *49*(20), e2021GL096816. https://doi.org/10.1029/2021GL096816

Guérin-Marthe, S., Nielsen, S., Bird, R., Giani, S., & Di Toro, G. (2019). Earthquake nucleation size: Evidence of loading rate dependence in laboratory faults. *Journal of Geophysical Research: Solid Earth*, *124*(1), 689–708. https://doi.org/10.1029/2018JB016803

Gulia, L., Tormann, T., Wiemer, S., Herrmann, M., & Seif, S. (2016). Short-term probabilistic earthquake risk assessment considering time-dependent b values. *Geophysical Research Letters*, *43*(3), 1100–1108. https://doi.org/10.1002/2015GL066686

Harbord, C. W. A., Nielsen, S. B., De Paola, N., & Holdsworth, R. E. (2017). Earthquake nucleation on rough faults. *Geology*, *45*(10), 931–934. https://doi.org/10.1130/G39181.1

Hirose, F., Tamaribuchi, K., & Maeda, K. (2021). Characteristics of foreshocks revealed by an earthquake forecasting method based on precursory swarm activity. *Journal of Geophysical Research: Solid Earth*, *126*(9), e2021JB021673. https://doi.org/10.1029/2021JB021673

Huang, H., Meng, L., Bürgmann, R., Wang, W., & Wang, K. (2020). Spatio-temporal foreshock evolution of the 2019 M 6.4 and M 7.1 Ridgecrest, California earthquakes. *Earth and Planetary Science Letters*, *551*, 116582. https://doi.org/10.1016/j.epsl.2020.116582

Hulbert, C., Rouet-Leduc, B., Johnson, P. A., Ren, C. X., Rivière, J., Bolton, D. C., & Marone, C. (2019). Similarity of fast and slow earthquakes illuminated by machine learning. *Nature Geoscience*, *12*(1), 69–74. https://doi.org/10.1038/s41561-018-0272-8

Johnson, P. A., Rouet-Leduc, B., Pyrak-Nolte, L. J., Beroza, G. C., Marone, C. J., Hulbert, C., et al. (2021). Laboratory earthquake forecasting: A machine learning competition. *Proceedings of National Academy of Science*, *118*(5), e2011362118. https://doi.org/10.1073/pnas.2011362118

Kagan, Y. Y. (2007). Simplified algorithms for calculating double-couple rotation. *Geophysical Journal International*, *171*(1), 411–418. https://doi.org/10.1111/j.1365-246x.2007.03538.x

Kanamori, H. (1981). The nature of seismicity patterns before large earthquakes. *Earthquake Prediction*, 1–19. https://doi.org/10.1029/ME004p0001

Karimpouli, S., Caus, D., Grover, H., Martínez-Garzón, P., Bohnhoff, M., Beroza, G. C., et al. (2023). Explainable machine learning for labquake prediction using catalog-driven features. *Earth and Planetary Science Letters*, *622*, 118383. https://doi.org/10.1016/j.epsl.2023.118383

Karimpouli, S. D., Kwiatek, G., Martínez-Garzón, P., Dresen, G., & Bohnhoff, M. (2024). Unsupervised clustering of catalog-driven features for characterizing temporal evolution of labquake stress. *Geophysical Journal International*. https://academic.oup.com/gji/advance-article/doi/10.1093/gji/ggae071/7616085

Kato, A., & Ben-Zion, Y. (2021). The generation of large earthquakes. *Nature Reviews Earth & Environment*, *2*(1), 26–39. https://doi.org/10.1038/s43017-020-00108-w

Kato, A., Obara, K., Igarashi, T., Tsuruoka, H., Nakagawa, S., & Hirata, N. (2012). Propagation of slow slip leading up to the 2011 Mw 9.0 Tohoku-Oki earthquake. *Science*, *335*(6069), 705–708. https://doi.org/10.1126/science.1215141

King, G. (1983). The accommodation of large strains in the upper lithosphere of the earth and other solids by self-similar fault systems: The geometrical origin of b-value. *Pure and Applied Geophysics*, *121*(5), 761–815. https://doi.org/10.1007/BF02590182

Kwiatek, G., Charalampidou, E.-M., Dresen, G., & Stanchits, S. (2014). An improved method for seismic moment tensor inversion of acoustic emissions through assessment of sensor coupling and sensitivity to incidence angle. *International Journal of Rock Mechanics and Mining Sciences*, *65*, 153–161. https://doi.org/10.1016/j.ijrmms.2013.11.005

Kwiatek, G., & Goebel, T. (2024). Acoustic emission and seismic moment tensor catalogs associated with triaxial stick-slip experiments performed on the Westerly Granite samples Dataset. *GFZ Data Services*. https://doi.org/10.5880/GFZ.4.2.2023.003

Kwiatek, G., Goebel, T. H. W., & Dresen, G. (2014). Seismic moment tensor and b value variations over successive seismic cycles in laboratory stick-slip experiments. *Geophysical Research Letters*, *41*(16), 5838–5846. https://doi.org/10.1002/2014GL060159

Kwiatek, G., Martínez-Garzón, P., Becker, D., Dresen, G., Cotton, F., Beroza, G. C., et al. (2023). Months-long seismicity transients preceding the 2023 MW 7.8 Kahramanmaraş earthquake, Türkiye. *Nature Communications*, *14*(1), 7534. https://doi.org/10.1038/s41467-023-42419-8

Kwiatek, G., Martínez-Garzón, P., & Bohnhoff, M. (2016). HybridMT: A MATLAB/shell environment package for seismic moment tensor inversion and refinement. *Seismological Research Letters*, *87*(4), 964–976. https://doi.org/10.1785/0220150251

Lasocki, S., & Papadimitriou, E. E. (2006). Magnitude distribution complexity revealed in seismicity from Greece. *Journal of Geophysical Research: Solid Earth*, *111*, B11. https://doi.org/10.1029/2005JB003794

Latour, S., Voisin, C., Renard, F., Larose, E., Catheline, S., & Campillo, M. (2013). Effect of fault heterogeneity on rupture dynamics: An experimental approach using ultrafast ultrasonic imaging. *Journal of Geophysical Research: Solid Earth*, *118*(11), 5888–5902. https://doi.org/10.1002/2013JB010231

Lebihain, M., Roch, T., Violay, M., & Molinari, J.-F. (2021). Earthquake nucleation along faults with heterogeneous weakening rate. *Geophysical Research Letters*, *48*(21), e2021GL094901. https://doi.org/10.1029/2021GL094901

Leeman, J. R., Marone, C., & Saffer, D. M. (2018). Frictional mechanics of slow earthquakes. *Journal of Geophysical Research: Solid Earth*, *123*(9), 7931–7949. https://doi.org/10.1029/2018JB015768

Legrand, D. (2002). Fractal dimensions of small, intermediate, and large earthquakes. *Bulletin of the Seismological Society of America*, *92*(8), 3318–3320. https://doi.org/10.1785/0120020025

Lei, X., & Ma, S. (2014). Laboratory acoustic emission study for earthquake generation process. *Earthquake Science*, *27*(6), 627–646. https://doi.org/10.1007/s11589-014-0103-y

Lippiello, E., Godano, C., & De Arcangelis, L. (2019). The relevance of foreshocks in earthquake triggering: A statistical study. *Entropy*, *21*, 173–182. https://doi.org/10.3390/e21020173

Lockner, D. (1993). The role of acoustic emission in the study of rock fracture. *International Journal of Rock Mechanics and Mining Science & Geomechanics Abstracts*, *30*(7), 883–899. https://doi.org/10.1016/0148-9062(93)90041-B

Lubbers, N., Bolton, D. C., Mohd-Yusof, J., Marone, C., Barros, K., & Johnson, P. A. (2018). Earthquake catalog-based machine learning identification of laboratory fault states and the effects of magnitude of completeness. *Geophysical Research Letters*, *45*(24), 13269–13276. https://doi.org/10.1029/2018GL079712

Main, I. G. (1991). A modified Griffith criterion for the evolution of damage with a fractal distribution of crack lengths: Application to seismic event rates and b-values. *Geophysical Journal International*, *107*(2), 353–362. https://doi.org/10.1111/j.1365-246X.1991.tb00830.x

Main, I. G. (1992). Damage mechanics with long-range interactions: Correlation between the seismic b-value and the fractal two-point correlation dimension. *Geophysical Journal International*, *111*(3), 531–541. https://doi.org/10.1111/j.1365-246X.1992.tb02110.x

Martínez-Garzón, P., Ben-Zion, Y., Abolfathian, N., Kwiatek, G., & Bohnhoff, M. (2016). A refined methodology for stress inversions of earthquake focal mechanisms. *Journal of Geophysical Research: Solid Earth*, *121*(12), 8666–8687. https://doi.org/10.1002/2016JB013493

Martínez-Garzón, P., Ben-Zion, Y., Zaliapin, I., & Bohnhoff, M. (2019). Seismic clustering in the Sea of Marmara: Implications for monitoring earthquake processes. *Tectonophysics*, *768*, UNSP 228176. https://doi.org/10.1016/j.tecto.2019.228176

Martínez-Garzón, P., Kwiatek, G., Bohnhoff, M., & Dresen, G. (2017). Volumetric components in the earthquake source related to fluid injection and stress state. *Geophysical Research Letters*, *44*(2), 800–809. https://doi.org/10.1002/2016GL071963

Martínez-Garzón, P., Kwiatek, G., Ickrath, M., & Bohnhoff, M. (2014). MSATSI: A MATLAB package for stress inversion combining solid classic methodology, a new simplified user-handling, and a visualization tool. *Seismological Research Letters*, *85*(4), 896–904. https://doi.org/10.1785/0220130189

Martínez-Garzón, P., Zaliapin, I., Ben-Zion, Y., Kwiatek, G., & Bohnhoff, M. (2018). Comparative study of earthquake clustering in relation to hydraulic activities at geothermal fields in California. *Journal of Geophysical Research: Solid Earth*, *123*(5), 4041–4062. https://doi.org/10.1029/2017JB014972

Marty, S., Schubnel, A., Bhat, H. S., Aubry, J., Fukuyama, E., Latour, S., et al. (2023). Nucleation of laboratory earthquakes: Quantitative analysis and scalings. *Journal of Geophysical Research: Solid Earth*, *128*(3), e2022JB026294. https://doi.org/10.1029/2022JB026294

McBeck, J., Aiken, J. M., Ben-Zion, Y., & Renard, F. (2020). Predicting the proximity to macroscopic failure in dynamic X-ray tomography triaxial compression experiments on rocks. *Earth and Planetary Science Letters*, *543*, 116344. https://doi.org/10.1016/j.epsl.2020.116344

McBeck, J., Ben-Zion, Y., & Renard, F. (2021). Fracture network localization preceding catastrophic failure in triaxial compression experiments on rocks. *Front. Earth Sci.*, *9*. https://doi.org/10.3389/feart.2021.778811

McBeck, J., Ben-Zion, Y., & Renard, F. (2022). Volumetric and shear strain localization throughout triaxial compression experiments on rocks. *Tectonophysics*, *822*, 229181. https://doi.org/10.1016/j.tecto.2021.229181

McLaskey, G. C. (2019). Earthquake initiation from laboratory observations and implications for foreshocks. *Journal of Geophysical Research: Solid Earth*, *124*(12), 12882–12904. https://doi.org/10.1029/2019JB018363

McLaskey, G. C., Kilgore, B. D., Lockner, D. A., & Beeler, N. M. (2014). Laboratory generated m-6 earthquakes. *Pure and Applied Geophysics*, *171*(10), 2601–2615. https://doi.org/10.1007/s00024-013-0772-9

Mclaskey, G. C., & Yamashita, F. (2017). Slow and fast ruptures on a laboratory fault controlled by loading characteristics. *Journal of Geophysical Research: Solid Earth*, *122*(5), 3719–3738. https://doi.org/10.1002/2016JB013681

Meng, H., & Fan, W. (2021). Immediate foreshocks indicating cascading rupture developments for 527 M 0.9 to 5.4 Ridgecrest earthquakes. *Geophysical Research Letters*, *48*(19), e2021GL095704. https://doi.org/10.1029/2021GL095704

Meredith, P. G., & Atkinson, B. K. (1983). Stress corrosion and acoustic emission during tensile crack propagation in Whin Sill dolerite and other basic rocks. *Geophysical Journal International*, *75*(1), 1–21. https://doi.org/10.1111/j.1365-246X.1983.tb01911.x

Mignan, A. (2011). Retrospective on the accelerating seismic release (ASR) hypothesis: Controversy and new horizons. *Tectonophysics*, *505*(1), 1–16. https://doi.org/10.1016/j.tecto.2011.03.010

Mignan, A. (2014). The debate on the prognostic value of earthquake foreshocks: A meta-analysis. *Scientific Reports*, *4*, 4099–4101. https://doi.org/10.1038/srep04099

Mizrahi, L., Nandan, S., Savran, W., Wiemer, S., & Ben-Zion, Y. (2023). Question-Driven ensembles of Flexible ETAS models. *Seismological Research Letters*, *94*(2A), 829–843. https://doi.org/10.1785/0220220230

Moisy, F. (2022). boxcount. MATLAB Central File Exchange. Retrieved from https://www.mathworks.com/matlabcentral/fileexchange/13063-boxcount

Morad, D., Sagy, A., Tal, Y., & Hatzor, Y. H. (2022). Fault roughness controls sliding instability. *Earth and Planetary Science Letters*, *579*, 117365. https://doi.org/10.1016/j.epsl.2022.117365

Mousavi, S. M., & Beroza, G. C. (2022). Deep-learning seismology. *Science*, *377*(6607), eabm4470. https://doi.org/10.1126/science.abm4470

Ogata, Y. (1999). Seismicity analysis through point-process modeling: A review. *Pure and Applied Geophysics*, *155*(2), 471–507. https://doi.org/10.1007/s000240050275

Ogata, Y., & Katsura, K. (2012). Prospective foreshock forecast experiment during the last 17 years. *Geophysical Journal International*, *191*(3), 1237–1244. https://doi.org/10.1111/j.1365-246X.2012.05645.x

Ohnaka, M. (1992). Earthquake source nucleation: A physical model for short-term precursors. *Tectonophysics*, *211*(1), 149–178. https://doi.org/10.1016/0040-1951(92)90057-D

Ohnaka, M., & Shen, L. (1999). Scaling of the shear rupture process from nucleation to dynamic propagation: Implications of geometric irregularity of the rupturing surfaces. *Journal of Geophysical Research: Solid Earth*, *104*(B1), 817–844. https://doi.org/10.1029/1998JB900007

Okubo, P. G., & Dieterich, J. H. (1984). Effects of physical fault properties on frictional instabilities produced on simulated faults. *Journal of Geophysical Research*, *89*(B7), 5817–5827. https://doi.org/10.1029/JB089iB07p05817

Picozzi, M., & Iaccarino, A. G. (2021). Forecasting the preparatory phase of induced earthquakes by recurrent neural network. *Forecasting*, *3*(1), 17–36. https://doi.org/10.3390/forecast3010002

Pierezan, J., & Dos Santos Coelho, L. (2018). *Coyote optimization algorithm: A new metaheuristic for global optimization problems* (pp. 1–8). 2018 IEEE Congress on Evolutionary Computation (CEC).

Ross, Z. E., Meier, M.-A., & Hauksson, E. (2018). P wave arrival picking and first-motion polarity determination with deep learning. *Journal of Geophysical Research: Solid Earth*, *123*(6), 5120–5129. https://doi.org/10.1029/2017JB015251

Rouet-Leduc, B., Hulbert, C., Lubbers, N., Barros, K., Humphreys, C. J., & Johnson, P. A. (2017). Machine learning predicts laboratory earthquakes. *Geophysical Research Letters*, *44*(18), 9276–9282. https://doi.org/10.1002/2017GL074677

Schoenball, M., Baujard, C., Kohl, T., & Dorbath, L. (2012). The role of triggering by static stress transfer during geothermal reservoir stimulation. *Journal of Geophysical Research: Solid Earth*, *117*, B9. https://doi.org/10.1029/2012JB009304

Scholz, C. H. (1968). The frequency-magnitude relation of microfracturing in rock and its relation to earthquakes. *Bulletin of Seismological Society of America*, *58*(1), 399–415. https://doi.org/10.1785/bssa0580010399

Schorlemmer, D., Wiemer, S., & Wyss, M. (2005). Variations in earthquake-size distribution across different stress regimes. *Nature*, *437*(7058), 539–542. https://doi.org/10.1038/nature04094

Schurr, B., Asch, G., Hainzl, S., Bedford, J., Hoechner, A., Palo, M., et al. (2014). Gradual unlocking of plate boundary-controlled initiation of the 2014 Iquique earthquake. *Nature*, *512*(7514), 299–302. https://doi.org/10.1038/nature13681

Scuderi, M. M., Collettini, C., & Marone, C. (2017). Frictional stability and earthquake triggering during fluid pressure stimulation of an experimental fault. *Earth and Planetary Science Letters*, *477*, 84–96. https://doi.org/10.1016/j.epsl.2017.08.009

Scuderi, M. M., Tinti, E., Cocco, M., & Collettini, C. (2020). The role of shear fabric in controlling breakdown processes during laboratory slow-slip events. *Journal of Geophysical Research: Solid Earth*, *125*(11), e2020JB020405. https://doi.org/10.1029/2020JB020405

Shreedharan, S., Bolton, D. C., Rivière, J., & Marone, C. (2021). Competition between preslip and deviatoric stress modulates precursors for laboratory earthquakes. *Earth and Planetary Science Letters*, *553*, 116623. https://doi.org/10.1016/j.epsl.2020.116623

Stanchits, S., Vinciguerra, S., & Dresen, G. (2006). Ultrasonic velocities, acoustic emission characteristics and crack damage of basalt and granite. *Pure and Applied Geophysics*, *163*(5–6), 975–994. https://doi.org/10.1007/s00024-006-0059-5

Sykes, L. R. (2021). Decadal seismicity prior to great earthquakes at subduction zones: Roles of major asperities and low-coupling zones. *International Journal of Geosciences*, *12*(09), 845–926. https://doi.org/10.4236/ijg.2021.129046

Tchalenko, J. S. (1970). Similarities between shear zones of different magnitudes. *GSA Bulletin*, *81*(6), 1625–1640. https://doi.org/10.1130/0016-7606(1970)81[1625:SBSZOD]2.0.CO;2

Trugman, D. T., & Ross, Z. E. (2019). Pervasive foreshock activity across southern California. *Geophysical Research Letters*, *46*(15), 8772–8781. https://doi.org/10.1029/2019GL083725

Varnes, D. J. (1989). Predicting earthquakes by analyzing accelerating precursory seismic activity. *Pure and Applied Geophysics*, *130*(4), 661–686. https://doi.org/10.1007/BF00881603

Vavryčuk, V. (2001). Inversion for parameters of tensile earthquakes. *Journal of Geophysical Research*, *106*(B8), 16339–16355. https://doi.org/10.1029/2001JB000372

Vavryčuk, V. (2014). Iterative joint inversion for stress and fault orientations from focal mechanisms. *Geophysical Journal International*, *199*(1), 69–77. https://doi.org/10.1093/gji/ggu224

Wiemer, S., & Wyss, M. (2000). Minimum magnitude of completeness in earthquake catalogs: Examples from Alaska, the Western United States & Japan. *Bulletin of Seismological Society of America*, *90*(4), 859–869. https://doi.org/10.1785/0119990114

Wu, C., Meng, X., Peng, Z., & Ben-Zion, Y. (2013). Lack of spatiotemporal localization of foreshocks before the 1999 Mw 7.1 Düzce, Turkey, earthquake. *Bulletin of the Seismological Society of America*, *104*(1), 560–566. https://doi.org/10.1785/0120130140

Wyss, M., Sammis, C. G., Nadeau, R. M., & Wiemer, S. (2004). Fractal dimension and b-value on creeping and locked patches of the san Andreas fault near Parkfield, California. *Bulletin of the Seismological Society of America*, *94*(2), 410–421. https://doi.org/10.1785/0120030054

Yamashita, F., Fukuyama, E., Xu, S., Kawakata, H., Mizoguchi, K., & Takizawa, S. (2021). Two end-member earthquake preparations illuminated by foreshock activity on a meter-scale laboratory fault. *Nature Communications*, *12*(1), 4302. https://doi.org/10.1038/s41467-021-24625-4

Yoshimitsu, N., Kawakata, H., & Takahashi, N. (2014). Magnitude −7 level earthquakes: A new lower limit of self-similarity in seismic scaling relationships. *Geophysical Research Letters*, *41*(13), 4495–4502. https://doi.org/10.1002/2014GL060306

Zaliapin, I., & Ben-Zion, Y. (2013a). Earthquake clusters in southern California I: Identification and stability. *Journal of Geophysical Research: Solid Earth*, *118*(6), 2847–2864. https://doi.org/10.1002/jgrb.50179

Zaliapin, I., & Ben-Zion, Y. (2013b). Earthquake clusters in southern California II: Classification and relation to physical properties of the crust. *Journal of Geophysical Research: Solid Earth*, *118*(6), 2865–2877. https://doi.org/10.1002/jgrb.50178

Zaliapin, I., & Ben-Zion, Y. (2016). A global classification and characterization of earthquake clusters. *Geophysical Journal International*, *207*(1), 608–634. https://doi.org/10.1093/gji/ggw300

Zaliapin, I., Gabrielov, A., Keilis-Borok, V., & Wong, H. (2008). Clustering analysis of seismicity and aftershock identification. *Physical Review Letters*, *101*(1), 018501. https://doi.org/10.1103/PhysRevLett.101.018501

Zang, A., Wagner, F. C., Stanchits, S., Dresen, G., Andresen, R., & Haidekker, M. A. (1998). Source analysis of acoustic emissions in Aue granite cores under symmetric and asymmetric compressive loads. *Geophysical Journal International*, *135*(3), 1113–1130. https://doi.org/10.1046/j.1365-246x.1998.00706.x